Marine and Petroleum Geology 135 (2022) 105382

Contents lists available at ScienceDirect

Marine and Petroleum Geology

journal homepage: www.elsevier.com/locate/marpetgeo

Permeability estimation of tight sandstone from pore structure characterization

Juncheng Qiao [a,b,c,**], Jianhui Zeng [a,b,*], Dongxia Chen [a,b], Jianchao Cai [a,b], Shu Jiang [c], Enzhao Xiao [d], Yongchao Zhang [e], Xiao Feng [f], Sen Feng [a,b]

[a] State Key Laboratory of Petroleum Resources and Prospecting, China University of Petroleum, Beijing, 102249, PR China
[b] College of Geosciences, China University of Petroleum, Beijing, 102249, PR China
[c] Key Laboratory of Tectonics and Petroleum Resources of Ministry of Education, School of Earth Resources, China University of Geosciences, Wuhan, 430074, China
[d] Key Laboratory for Polar Science, MNR, Polar Research Institute of China, Shanghai, 200136, China
[e] The Key Laboratory of Gas Hydrate, Ministry of Natural Resources, Institute of Marine Geology, Qingdao, 266071, China
[f] CNPC Engineering Technology R&D Company Limited, Beijing, 102206, China

ARTICLE INFO

Keywords:
Permeability estimation
Tight sandstone
Pore structure type
Pore connectivity
Microscopic heterogeneity

ABSTRACT

Permeability, a crucial parameter in the subsurface geological and industrial activities, is highly heterogeneous in tight sandstone. Great difficulties and accuracy losses present in the permeability estimation of tight sandstone owing to its intricate pore structures. In this paper, to obtain reliable permeability estimation models for tight gas sandstone, the popular Coates, Schlumberger Doll Research, and Pittman models are improved from a systematic pore structure characterization. The characterization, integrating multiple techniques and incorporating percolation theory and fractal model, identifies the presences of three pore structure types, involving the mixed pore type, single-pore dominant type, and dual porous type. Attribute differences are discovered in the pore constitute, size distribution, microscopic heterogeneity, and connectivity of different structure types, in which disparate structural variation rules are identified in the pore-controlled and dual porous structures. These differences are responsible for the distinctions in the continuous fluid percolation pathways. The pore-controlled sandstone shares similar reticular networks with variations in extension degrees, while the dual porous sandstone exhibits a completely different tubular network, indicating different permeability variation mechanisms. Differed correlation trends between pore attributes and permeability in pore-controlled and dual porous tight sandstone suggest that permeability is primarily affected by pore structure type, followed by connectivity. The permeability of pore-controlled tight sandstone is determined by the pore geometrical features and influenced by connectivity and heterogeneity, while that of dual porous one is controlled by the attributes of micro cracks. Modification is performed on the Coates, SDR, and Pittman models by taking pore structures, particularly the structure types and connectivity, into account. Evident performance enhancements occur in these calibrated models. The excellent applicability of the improved models in pore-controlled tight sandstone confirms that pore structural types should be addressed in priority, followed by pore connectivity, in the permeability estimation of tight sandstone.

1. Introduction

Permeability has been always recognized as a key parameter in the formation and reserve evaluations of hydrocarbon reservoirs and geothermal reservoirs as well as aquifers since it exhibits direct relations to the fluid flow and hydrocarbon deliverability in natural porous media (Thomas and Ward, 1972; Deutsch, 1989; Pittman, 1992; Pape et al., 1999; Arns et al., 2005; Zha et al., 2017). It becomes more crucial in tight sandstone owing to the reservoir heterogeneity. Permeability is commonly considered as a macroscopic description of pore structure and generally has functional correlations with pore structure properties (Bourbie and Zinszner, 1985; Jacquin and Adler, 1987; Lock et al., 2002; Rezaee et al., 2012; Mao et al., 2013; Sheng et al., 2020). As it is impractical to measure the in-situ absolute permeability from the

* Corresponding author. State Key Laboratory of Petroleum Resources and Prospecting, China University of Petroleum, Beijing, 102249, PR China.
** Corresponding author. State Key Laboratory of Petroleum Resources and Prospecting, China University of Petroleum, Beijing, 102249, PR China.
E-mail addresses: Juncheng.Qiao@cup.edu.cn (J. Qiao), zengjh@cup.edu.cn (J. Zeng).

https://doi.org/10.1016/j.marpetgeo.2021.105382
Received 25 November 2020; Received in revised form 11 October 2021; Accepted 12 October 2021
Available online 14 October 2021

wellbore, predicting permeability using its correlations to other petrophysical properties or pore structure parameters has been brought to forefront in the formation evaluation (Wong et al., 1984; Johnson et al., 1986; Banavar and Schwartz, 1987; Daigle and Dugan, 2009; Yao et al., 2010; Zhao et al., 2016), particularly in the tight sandstone reservoirs with extremely complicated pore structures (Rezaee et al., 2012; Zhao et al., 2016).

Numerous permeability estimation models have been developed on the basis of electrical conductivity (Wong et al., 1984; Liang et al., 2000; Arns et al., 2001; Zisser et al., 2010), mercury intrusion porosimetry (MIP) (Purcell, 1949; Thomeer, 1960; Wells and Amaefule, 1985 Pittman, 1992; Rezaee et al., 2012), NMR response, and other petrophysical data. The existing models could be divided into four categories. One of the popular approaches is obtained based on the Poiseuille equation, in which the porous media is simplified as cylindrical tubes with different radii (Purcell, 1949; Kolodzie Jr, 1980; Swanson, 1981; Thomeer, 1983; Wells and Amaefule, 1985). Since the Purcell model was proposed by combining the Poiseuille equation and Darcy law (Purcell, 1949), it has been modified by Thomeer model that approximated the mercury injection data as a hyperbola and related the hyperbolic functions to permeability (Thomeer, 1983). Swanson (1981) further indicated that the apex of the hyperbola corresponds to the maximum ratio of mercury intrusion saturation to capillary pressure ($(S_{Hg}/P_C)_{apex}$, Swanson parameter), and correlated it to the permeability. The Swanson model has been extended by Guo et al. (2004) by applying the capillary parachor. Liu et al. (2016) improved this model by introducing the porosity into it. The second category originates from the percolation theory. Following the percolation arguments considering that the fluid percolation in the system with very wide distributions of local conductances is controlled by the largest conductances that form the spanning pathways across the system, the permeability of sedimentary rocks can be correlated to critical path diameter in the K-T model (Katz and Thompson, 1986). The third category employing the empirical approach includes the Kozeny-Carman model (Kozeny, 1927; Carman, 1997), Windland model (Zhao et al., 2015), Pittman model (Pittman, 1992), Nelson model (Nelson, 1994), and recent other models modified from these models, most of which were built by using the multiple linear regression analysis (MLR) (Rezaee et al., 2012; Zhao et al., 2016). The fourth category stems from the relationship between the relaxation measurements of NMR and permeability (Chang et al., 1994; Kleinberg, 1996; Coates et al., 1999; Daigle and Dugan, 2009), mainly including the Coates model (Coates et al., 1999) and SDR (Schlumberger Doll Research) model (Xiao et al., 2012), which are applicable in the formation containing water and/or hydrocarbons and in the formation only containing water, respectively (Rezaee et al., 2012). Additionally, numerical simulation that utilizes the pore images acquired by casting thin section (CTS), scanning electron microscopy (SEM), and X-ray computed tomography (X-CT) emerges as another effective approach (Adler et al., 1990; Spanne et al., 1994; Ferreol and Rothman, 1995; Arns et al., 2001, 2004, 2005).

As most of the permeability prediction models were developed for conventional sandstone and carbonate rock, pitfalls appear when these models are directly applied to the tight rocks with extremely wide pore size distributions (PSD) and heterogeneous pore structures (Rezaee et al., 2012; Zhao et al., 2016). On one hand, the simplification of the complex porous media neglects pore connectivity that is key for the fluid flow in tight sandstone (Cai et al., 2014; Tiab and Donaldson, 2015; Xiao et al., 2017b; Ghanbarian et al., 2019). On the other hand, the deficiencies in the pore structure characterization of tight rocks lead to inaccuracies in the determination or approximation of the critical path diameter and geometric or harmonic mean (Katz and Thompson, 1986; Arns et al., 2005; Hunt et al., 2014), resulting in estimation deviations (Qiao et al., 2020a). Notably, as most of the popular models were derived from the MIP, which has shortcomings in probing the overall pore structure of tight rocks due to the shielding effects and grain compression (Clarkson and Bustin, 1996; Kaufmann et al., 2009), it is evident that these models will be limited in the applications to tight sandstone. Additionally, the tight sandstone presents pictures of extreme in the correlations between pore structure properties and permeability due to the extensive compaction and diagenetic modification (Soeder and Chowdiah, 1990; Desbois et al., 2011; Lai et al., 2016b, 2018; Qiao et al., 2020b). As indicated, the proper permeability estimation of tight sandstone strongly relies on a systematic pore structure characterization and must incorporate the pore structure attributes (e.g. pore sizes, shapes, and connectivity), of which pore connectivity is of vital importance (Cai et al., 2014; Ghanbarian et al., 2019).

To measure the pore structure properties of tight sandstone, various techniques have been employed, including the fluid-invasion techniques, image-based techniques (Chalmers et al., 2012; Bultreys et al., 2016; Wang et al., 2016; Yang et al., 2016a), gas absorption techniques (Ross and Bustin, 2007, 2009; Clarkson et al., 2013), and radiation techniques (e.g. nuclear magnetic resonance (NMR) (Gallegos et al., 1987; Gallegos and Smith, 1988; Yao et al., 2010; Lai et al., 2016a; Zhao et al., 2017) and X-CT (Mees et al., 2003; Blunt et al., 2013; Cnudde and Boone, 2013)). However, each technique is limited in probing the overall pore structure of tight sandstone (Yuan and Swanson, 1989; Clarkson and Bustin, 1996; Kaufmann et al., 2009; Yao and Liu, 2012; Al Hinai et al., 2014; Zhao et al., 2015; Wu et al., 2017; Huang et al., 2018; Qiao et al., 2020a, 2020d). Especially, the inherent shortcoming of MIP in the pore size and connectivity measurements is responsible for the pitfalls in the applications of the popular permeability estimation models in tight sandstone (Yao and Liu, 2012; Zhao et al., 2015; Wu et al., 2017; Qiao et al., 2020a). Some attempts have been made to integrated complementary techniques to overcome these shortcomings (Sok et al., 2010; Clarkson et al., 2013; Wang et al., 2014; Zhao et al., 2015; Wu et al., 2017; Qiao et al., 2020a). Comparing these integrations, the combination of the non-destructive techniques, i.e. NMR and X-CT (Yao et al., 2009, 2010), which could overcome the potential destruction risks and deficiencies in the pore size and connectivity measurements, is believed to provide a solid basis of pore structure information.

Permeability estimation of tight sandstone is of great importance for the exploration and development of energy resources, but it is very challenging. Considering the current issues, in the presented paper, a systematic pore structure characterization is firstly conducted on the Upper Paleozoic Permian tight sandstone in the Ordos Basin by integrating porosity and permeability measurements, CTS, SEM, X-CT, and NMR to probe the overall pore structure attributes. The popular models, i.e. Coates model and SDR model based on NMR and empirical approach on the basis of PSD (i.e. Pittman model), are examined and modified by taking the pore structure attributes into consideration. Integrated analyses give out the main goal of our study, to develop reliable permeability estimation models for tight sandstone under constrain of pore structure.

This paper tries to provide comprehensive understandings for the pore structure and its correlation to permeability, and reliable permeability estimation models in tight sandstone. This work may also enlighten associated permeability works in aquifers or soils.

2. Sample information and methodology

2.1. Sample information and pretreatment

The sampling was conducted on the tight formations in the Upper Paleozoic Permian strata in the Tabamiao area in the northeastern of the Ordos Basin (Fig. 1A–C), the second largest sedimentary basin of China (Johnson et al., 1989; Zhao et al., 2020). The tight sandstone, interbedded with siltstone or mudstone in the Shanxi Formation, is characterized by low porosity (5–10%) and ultralow permeability (0.01–060 mD), and exhibits intense reservoir quality heterogeneity, bringing extreme difficulties to the petrophysical property prediction (Liu et al., 2015; Yang et al., 2016b; Qiao et al., 2019a, 2020c).

Ten samples, cylindrical core plugs with diameters of ~1.0 inch and lengths of ~2.0 inch, were prepared from the fresh cores (Table 1). The

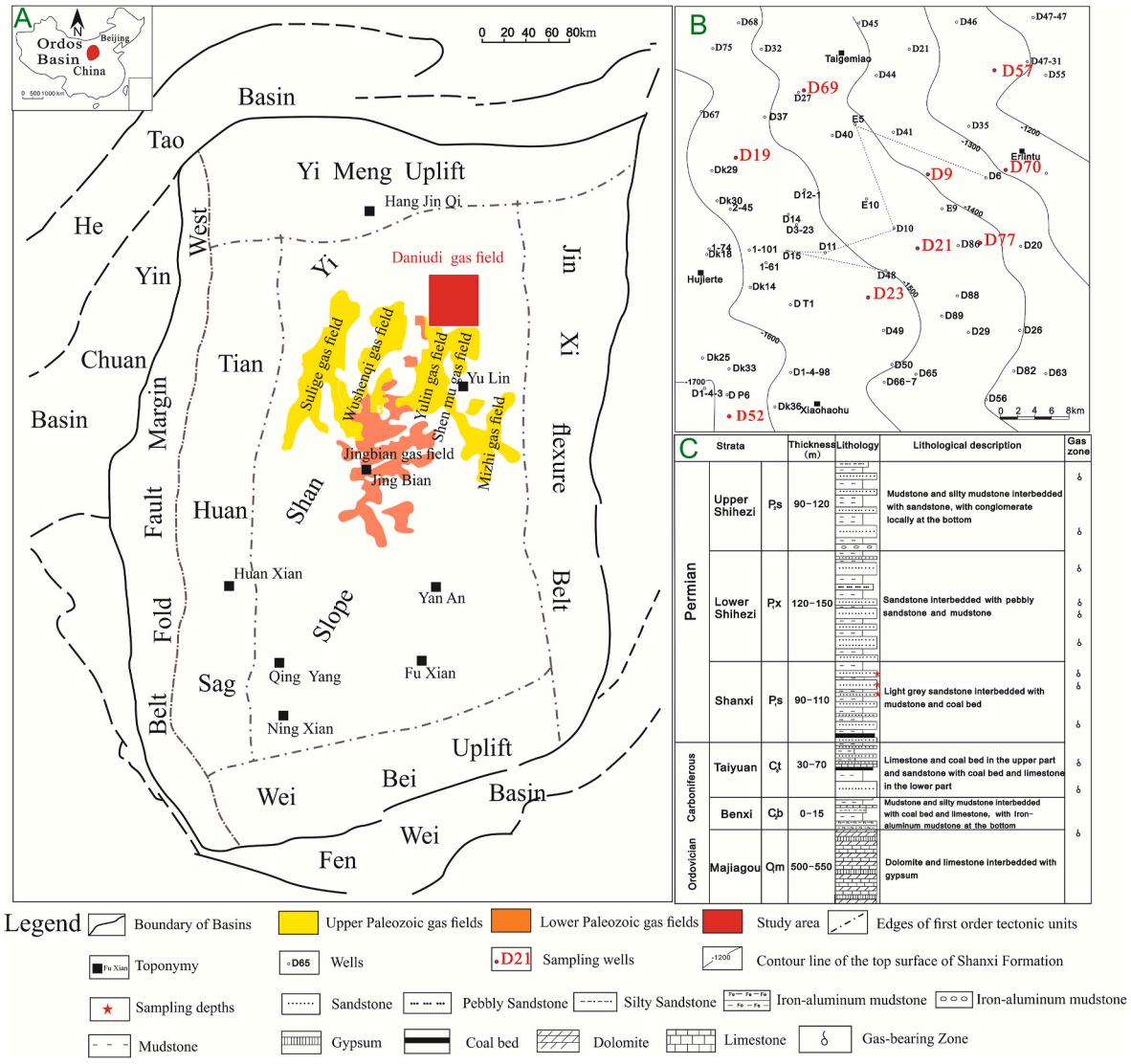

Fig. 1. (A) Simplified tectonic units of the Ordos Basin and location of study area. (B) Contour map of the top surface of Shanxi Formation. (C) Stratigraphic column of the upper Paleozoic tight gas system and location of the sampling.

Table 1
Sample information.

Sample	Depth (m)	Formation	Length (cm)	Diameter (cm)	Porosity (%)	Permeability (mD)
D19-8	2751.60	Shanxi	5.04	2.44	1.05	0.041
D69-19	2691.20	Shanxi	5.23	2.42	1.46	0.074
D23-3	2690.90	Shanxi	5.00	2.45	1.84	0.088
D21-1	2642.58	Shanxi	4.93	2.43	3.22	0.312
D9-15	2584.00	Shanxi	5.04	2.42	4.66	0.343
D77-23	2575.45	Shanxi	4.96	2.44	7.49	0.557
D69-20	2685.60	Shanxi	4.93	2.42	5.05	0.669
D23-4	2706.00	Shanxi	5.02	2.42	7.55	0.670
D57-6	2578.53	Shanxi	4.99	2.42	13.04	0.820
D70-12	2433.86	Shanxi	5.01	2.45	4.49	1.966

samples, lithic sandstone in origin, are fine-to medium-grained, covering the major types of reservoir rocks in the Shanxi Formation. Before testing, the impurity and residual hydrocarbon were removed from the cores before they were dried for 48 h under a temperature of 110 °C. Porosity and permeability measurements were performed on the cores using a CMS-300 instrument in the State Key Laboratory of China University of Petroleum Beijing, the porosity and Klinkenberg permeability were probed by helium expansion method and pressure transient method (confining pressure of ~1.5 MPa), respectively. The plugs were then cut into three sub parts along the longitudinal, two of them with lengths of 5 mm were prepared for the CTS and SEM, respectively, and the other one with length of 2.50 cm was remained for NMR and X-CT analyses.

2.2. Experimental method

2.2.1. CTS and SEM

CTS, impregnated by blue epoxy resin, were observed using an FEI optical microscope, from which the pore types, pore fillings, and pore long dimensions were directly observed and estimated. Point counting method was employed to approximate constitutes of different pore types with a standard deviation of approximately 3% on the collected micrographs.

SEM was used to complement the observations of pore morphologies and interstitial filling occurrences of tiny pores that could not be well detected by the CTS. Thin slices of 1.0 mm in thicknesses, mechanically polished, were golden-coated before experiments. Following observation was performed employing an FEI Quanta 400F instrument with highest resolution of 1.0 nm, with dozens of secondary imaging micrographs collected.

2.2.2. NMR

NMR measurements were performed on the plugs of 2.50 cm in lengths using the Recore-04 low-field NMR spectrometer with a resonance frequency of 2.38 Mhz. The test set echo time and number to 0.15 ms and 5000, respectively, a waiting time to 2 s, and scanning times to 32, following the Chinese testing standard SY/T 6490–2014. Carr-Purcell-Meiboom-Gill (CMPG) sequence was utilized to acquire T_2 relaxation time. Before the tests, the sub plugs were dried for another 24 h under a drying temperature of 110 °C and weighed by electronic balance. Then the sub samples were saturated with $CaCl_2$ solution with a salinity of 50 g/L, corresponding to the actual brine types and salinity of the formation water in the Shanxi formation, after the atmosphere in the plugs was evacuated by a vacuum pump for 24 h. The first-time NMR measurement was conducted to obtain the T_2 spectrums of the saturated samples (T_{2s}) after the wet weights of the samples were measured. The samples underwent a second-time NMR test after a 1 h centrifugal process with centrifugal pressure of 300 Psi, from which the T_2 spectrums of the centrifugal samples were derived (T_{2c}).

2.2.3. X-CT

Impurities removal and 48 h drying (temperature of 110 °C) were conducted on the plugs that have underwent NMR measurements before the X-CT tests were performed on the Zeiss Xradia 510 Micro-CT (highest resolution of 650 nm). To guarantee the good X-ray penetration and imaging, the scanning voltage was set to 100 Kev and current was set to 90 μA with scanning resolution of 3.0 μm and exposure time of 2.0 s. Hundreds of tomography images were acquired after the original scanning data was immediately reconstructed to three-dimensional (3D) hexadecimal grayscale images. A reliable representative voxel of 500 pixel × 500 pixel × 500 pixel was cropped from the reconstructed images for further investigation. Segmentation, aiming to extract pore spaces from the rock matrix, was proceeded by the FEI AvizoFire 9.0.2 according to the X-Ray attenuation differences in materials with varied density following the Bill law. Following pore separation and successive pore network modelling (PNM) based on the maximum spherical algorithm provided the detailed pore structure parameters (e.g. pore size, volume, and coordination number), whose methodology has been thoroughly reported by Dong et al. (2009) in detail.

2.3. Choice and modification of permeability estimation model

Plenty of permeability estimation models have been proposed using the MIP and NMR data, of which the Swanson model modified from Thomeer model, Pittman model modified from Windland model based on empirical approaches using the PSD, Coates model on the basis of the ratio between movable and irreducible fluids, and SDR model based on the geometric mean of T_2 distributions are most frequently invoked (Kolodzie Jr, 1980; Swanson, 1981; Pittman, 1992; Coates et al., 1999). The Coates, SDR, and Pittman models were chosen in our study considering the data acquired, while the Swanson model was excluded owing to its strong dependence on the mercury porosimetry. The performances of Coates and SDR models were reevaluated based on the combination of NMR and X-CT measurements, while that of the Pittman model was evaluated on the basis of the PSDs derived from X-CT. However, the performances of the chosen models are still restricted. On one hand, almost all of the models were primarily developed for the conventional rocks (Rezaee et al., 2012; Xiao et al., 2017b), whose permeability is more homogeneous and greater than tight sandstone. On the other hand, pore structure simplification and incomplete PSDs probed by MIP result in further poor performances (Cai et al., 2014; Tiab and Donaldson, 2015; Qiao et al., 2020a). Additionally, some key parameters (e.g. porosity) used in the current models may not be directly applied to tight sandstone. Therefore, the chosen models should be modified considering the experimental methods, data, and intricate pore structures of tight sandstone.

For the Coates model, recent publications argued that the ratio of free fluid index (FFI) to bound volume of irreducible water (BVI) (FFI/BVI) should be calibrated in tight sandstone. Some authors have reported that the cutoff value used in the determination of FFI and BVI of tight sandstone should be established according to the factual NMR measurements rather than just simply employ the default $T_{2cutoff}$ value of 33 ms (Ge et al., 2014; Westphal et al., 2005). More importantly, the thin movable water films that present in the pore spaces with T_2 less than the cutoff value and immovable water films present in the pores with T_2 greater than the cutoff value in tight sandstone (Dai et al., 2016; Lai et al., 2018; Huang et al., 2018; Qiao et al., 2020d), belonging to the potential movable water layer in the capillary bound water zone of small pores and strongly immovable water layer in the clay bound water zone of large pores, respectively, are neglected in the common constraint bound water model but should be highlighted according to the clay bound water concepts (Bouton et al., 1996; Churaev, 2003; Yuan et al., 2018; Yuan and Rezaee, 2019a) under the condition that the bound water cloud not be fully centrifuged (Lonnes et al., 2003; Martin and Dacy, 2004). Current research indicates a better applicability of clay bound water model, taking the movable capillary bound fluids in the pores with T_2 less than the cutoff value and immovable clay bound fluids in the pores with T_2 greater than the value into account, in the evaluation of movable fluid saturation (S_{mw}) and irreducible fluid saturation (S_{iw}) (Huang et al., 2018; Qiao et al., 2020). Accordingly, the FFI/BVI in the Coates model is modified by the ratio of S_{mw} and S_{iw} (S_{mw}/S_{iw}). Additionally, the porosity used in the model should be calibrated by taking the pore structure attributes into account, especially the pore connectivity, which will be discussed in the later sections. The porosity is the only concern in the modification as the T_2 geometric mean is directly obtained from the NMR measurements in the SDR model. For the Pittman model, the r_i that yields best correlation with permeability is much smaller than the conventional sandstone (r_{35}) (Rezaee et al., 2012). Moreover, it is indicated that more groups of MLR with a smaller saturation interval are required when employing the model to tight gas sandstone. Thus, incremental saturation or pore volume percentage interval of 5%, recognized by recent studies (Zhao et al., 2015), and incremental saturation or pore volume percentage range of 5–50%, are adopted in the modification.

To examine the performances of the original and modified estimation models, both of the determination coefficient (R^2) and adjusted determination coefficient (R_{adj}^2) are introduced to this case of study. They have been widely employed in permeability estimation and are believed to be the most reliable indicators for accuracy comparison (Zhao et al., 2016).

3. Results

3.1. Porosity, permeability, and pore types in origin

The samples investigated are characterized by low porosity and

ultralow permeability, of which the measured helium porosity and Klinkenberg permeability range from 1.05 to 13.04% (avg. 4.98%) and from 0.074 to 1.966 mD (0.554 mD), respectively. Significant variations present in different samples, covering the majority of the porosity and permeability ranges of tight sandstone, which provides a solid data basis for the permeability estimation. Notably, the sample D70-12 exhibits low porosity but abnormal high permeability of 1.966 mD, which is probably attributed to presences of the micro cracks (MC). A similar condition happens in the sample D69-20.

There are five types of pores in origin, including the primary residual intergranular pores (P-interP), dissolution intergranular pores (D-interP), dissolution intragranular pores (D-intraP), intercrystalline pores (interC), and MC (Fig. 2). The P-interPs, preserved after compaction, generally show regular outlines, flat edges, and long dimensions ranging from dozens of microns to hundreds of microns (Fig. 2B). The D-interPs are normally generated from the dissolution along the edges between the intergranular pores and rock grains (e.g. feldspar and rock fragments), succeeding the original appearances of the intergranular pores or grains but exhibit strongly curved edges (Qiao et al., 2020c) (Fig. 2C). Their sizes vary from several microns to hundreds of microns, determined by the dissolution degrees. The D-intraPs, formed from the particle dissolution, are characterized by irregular shapes and smaller sizes ranging from hundreds of nanometers to dozens of microns, exhibiting particular orientations in feldspar but showing irregular orientations in rock fragments (Fig. 2C). The InterCs are the small spaces among the clay aggregates, with widths of several to hundreds of nanometers, their shapes are closely related to the inner structure of the clay minerals (Fig. 2D). The MCs, slit pores with widths between hundreds of nanometers and dozens of microns, and lengths of hundreds of microns, generally run through the fragile grains and interconnect the pores, resulting in evident increases in pore connectivity but no obvious increases in plane-viewed pore volumes (Fig. 2C and F).

3.2. NMR results

The NMR T_2 spectrums acquired before and after centrifugation and their characteristic parameters are displayed in Fig. 3 and shown in Table 2, respectively. The tight sandstone samples exhibit wide T_{2s}, ranging from 0.1 to 1000 ms, with T_2 cutoffs between 3.4 and 41.5 ms and T_2 geometric means between 1.71 and 41.27 ms. Although it is hard to convert the T_2 to pore size owing to the difficulties in determining the surface relaxation ratio resulted from the absences of MIP and gas absorption techniques in this study, it can also be inferred that the tight sandstone is characterized by wide PSD since the strong internal correlation between pore size and T_2 (Yuan and Rezaee, 2019b). The T_{2s} distributions are dominated by Gaussian distribution, followed by bimodal distribution, suggesting presences of multiple-scale pores. With the increase of permeability from sample D19-8 to D70-12, the T_{2s} distributions become fluctuated. The T_{2s} of the tight sandstone with permeability <0.1 mD is characterized by Gaussian distributions, with peaks in the interval of 0.1–10 ms and peak values of approximately 1.0 ms, indicating the dominant contribution of small pores to porosity (Fig. 3A–C). The amplitudes of T_{2s} in the samples with permeability >0.1 mD increase evidently in the interval of 10–1000 ms, exhibiting secondary peaks in the range 100–1000 ms, indicating increases in the porosity contributions of large pores or MCs (Fig. 3C–J). Notably, the evident bimodal distribution patterns and high amplitudes of the right peak in the sample D21-1 and D69-20 are attributed to the porosity contribution increases of the P-interGs, D-interGs, and MCs. However, the increasing presences of MCs in the D69-20 are responsible for the differences in the T_{2s} spectrums of the two samples.

The relationships between the T_{2s} and T_{2c} are normally used to identify the movable and irreducible fluids, in which the T_{2c} generally has lower amplitudes than T_{2s} (Fig. 3). The signal amplitude differences between the two spectrums suggest the movable fluids in certain-sized pores, and signal amplitudes of T_{2c} represent the irreducible fluids trapped in them. The amplitude differences rise with T_2 values, while the amplitudes of T_{2c} decrease, suggesting rising contents of movable fluids from small pores to large pores and better connectivity of the large pores (Fig. 3). With decreasing permeability, the amplitude differences become narrower, especially in the pores with longer T_2. Generally, the total movable fluid contents reduce and pores with same radii exhibit lower movable fluid proportions, indicating losses in the fluid mobility and connectivity of all sizes of pores (Fig. 3G–A). The residual fluids in the pores are probably attributed to the presence of clay bound water or capillary bound water in the laminar or fibrous clay aggregates, whose contents rise with decreasing permeability. However, the sharp increases of intergranular pores and MCs in the sample D21-1 and D69-20

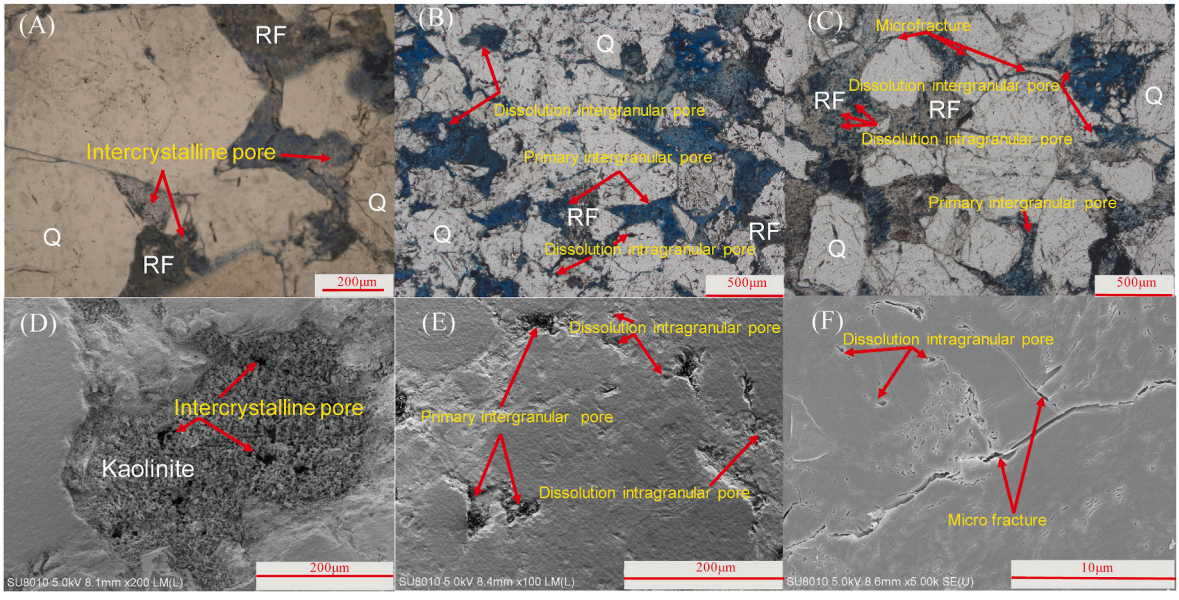

Fig. 2. Pore types, locations, and constitutes observed by CTS and SEM. Intercrystalline pores dominate the plane-viewed porosity of the sample D19-8 (A) and (D). Plane-viewed porosity originates from primary and dissolution intergranular pores, followed by intragranular pores in the sample D57-6 (B) and (E). Pore system comprises dissolution intergranular and intragranular pores, primary intergranular pores, intercrystalline pores, and micro cracks in the sample D70-12 (C) and (F).

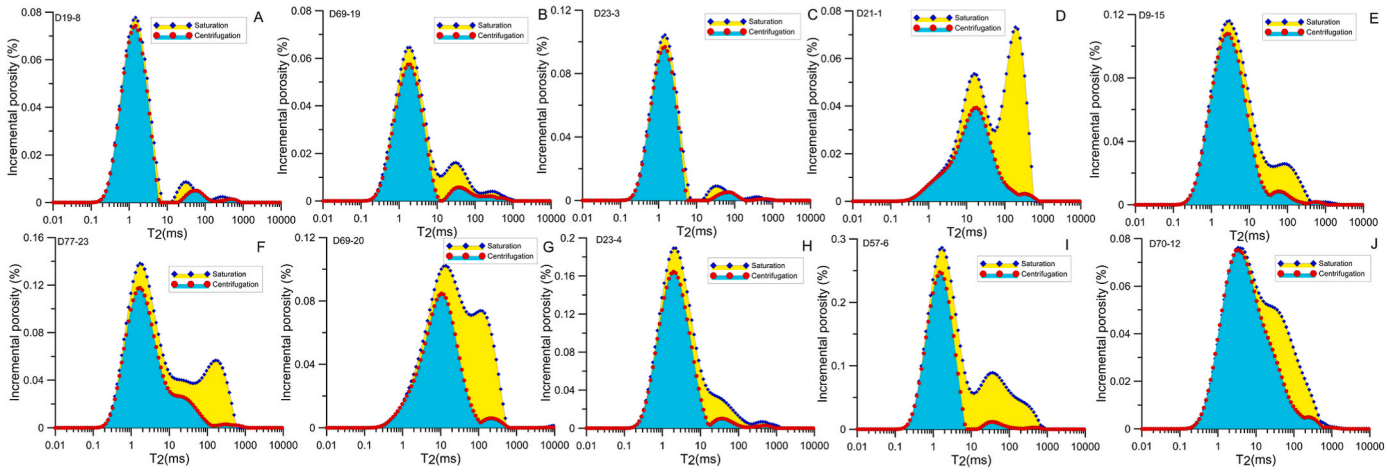

Fig. 3. T_2 spectrums before and after centrifugation of ten tight sandstone samples.

Table 2
NMR results.

Sample	$T_{2cutoff}$ (ms)	T_{2gm} (ms)	FFI (%)	BVI (%)	S_{mw} (%)	S_{iw} (%)	NMR porosity (%)	Movable porosity (%)	Irreducible porosity (%)
D19-8	4.50	1.83	11.23	88.77	10.68	89.32	2.34	0.25	2.09
D69-19	5.54	3.40	25.90	74.10	25.10	74.90	2.47	0.62	1.85
D23-3	3.40	1.71	14.44	85.56	13.16	86.84	3.04	0.40	2.64
D21-1	33.70	41.27	54.11	45.89	53.18	46.53	3.46	1.84	1.61
D9-15	11.89	5.14	23.31	76.69	22.72	77.28	5.37	1.22	4.15
D77-23	9.01	6.60	35.46	64.51	35.12	64.88	6.92	2.43	4.49
D69-20	25.52	22.20	44.58	55.42	27.39	55.80	5.95	2.63	3.32
D23-4	5.54	3.34	26.59	73.41	25.10	74.90	7.45	1.87	5.58
D57-6	3.40	4.68	42.69	57.31	42.68	57.32	12.30	5.25	7.05
D70-12	41.50	9.87	21.18	78.82	20.97	79.03	4.53	0.95	3.58

Note that $T_{2cutoff}$ = the cutoff value of T_2 distribution, T_{2gm} = the geometric mean of T_2 distribution, FFI = free fluid index, BVI = bulk volume of irreducible water, S_{mw} = movable water saturation evaluated by clay bound water model, and S_{iw} = irreducible water saturation evaluated by clay bound water model.

result in fluid mobility and connectivity increases of the pore system. There are two ways to calculate the movable fluid saturation, one of which is based on the $T_{2cutoffs}$ and has been thoroughly explained by Coates et al. (1999). The FFI calculated on the basis of $T_{2cutoffs}$ ranges from 11.23 to 54.11% (avg. 29.95%) and the BVI is in the range 45.89–88.77% (70.05%) (Table 2). The other approach is proposed on the basis of the clay bound water concept (Lonnes et al., 2003; Martin and Dacy, 2004; Huang et al., 2018) that takes the movable capillary bound water in the pores with radii less than cutoff values and immovable clay bound water in the pores with radii greater than the values into account, of which the movable fluid saturation is calculated using the ratio of the covering area between T_{2s} and T_{2c} to covering area of T_{2s} (Qiao et al., 2020c, 2020d). The S_{mw} ranges from 10.68 to 53.18% (avg. 27.61%), exhibiting increasing trends with permeability. The movable porosity is obtained by multiplying NMR porosity and S_{mw}, which is in the range of 0.25–5.25% with a mean of 1.65% (Table 2). The S_{iw} and irreducible porosity are calculated and listed in Table 2. Abnormal deviations occur in the relationships between FFI, S_{mw}, and permeability of the samples D70-12 and D69-20. They are characterized by high permeability but low FFI and S_{mw} (Table 2). The deviation implies that the pore structure should be emphasized in the permeability prediction except the choices of the parameters describing the fluid mobility.

3.3. X-CT results

The three dimensional (3D) grayscale images, binary images showing the pores extracted from rock matrix, and color-labelled images displaying pore system connectivity derived from X-CT scanning are illustrated by three representative samples D23-3, D57-6, and D70-12 in Fig. 4. The white areas, white grey areas, dark grey areas, and dark areas in the grayscale images separately represent the carbonate induced cements or K-feldspar, framework grains (e.g. albite, quartz, and rock fragments), clay minerals, and pore spaces (Liu et al., 2017; Qiao et al., 2020c) (Fig. 4A–C). The blue labelled regions in the transformed binary images show the pore spatial distribution (Fig. 4D–F), and they are further separated and labelled by different colors to exhibit the pore system connectivity, in which the same color indicates interconnected pores, and different colors suggest disconnected or poorly connected pores (Fig. 4G–I). Detailed pore structure parameters obtained, e.g. average pore surface area, volume, radius, and coordination number, are listed in Table 3.

From the results, we can figure out that the tight sandstone is characterized by more complicated matrix and pore system than the standard Berea sandstone (Liu et al., 2017), showing smaller average pore radius of 7.93 μm, average pore volume of 72609.89 μm^3, and worse pore connectivity. As shown in Fig. 4, the interconnected large pores, generally labelled by single color and occupying greater spaces, are minor in quantity but are dominant in volume. They form bulky pore clusters and construct the major structure of the system (Fig. 4G–I). They are deduced to be P-interPs and D-interPs in origin when comparing their sizes, locations, and geometrical shapes with the CTS and SEM observations (Fig. 2B, C, E). The relative small pores closely related to D-intraPs pores distribute nearby the large pore clusters (Fig. 4H), while the numerous tiny pores, mostly InterCs in origin, show poor connectivity and are characterized by plenty of color labels covering minor volumes. One part of these pores locate inside or between the pore clusters, while the other part distributes away from the major structure (Fig. 4G), which are determined by the filling locations and patterns of the clay aggregates. The dominant roles of large pores in volume and

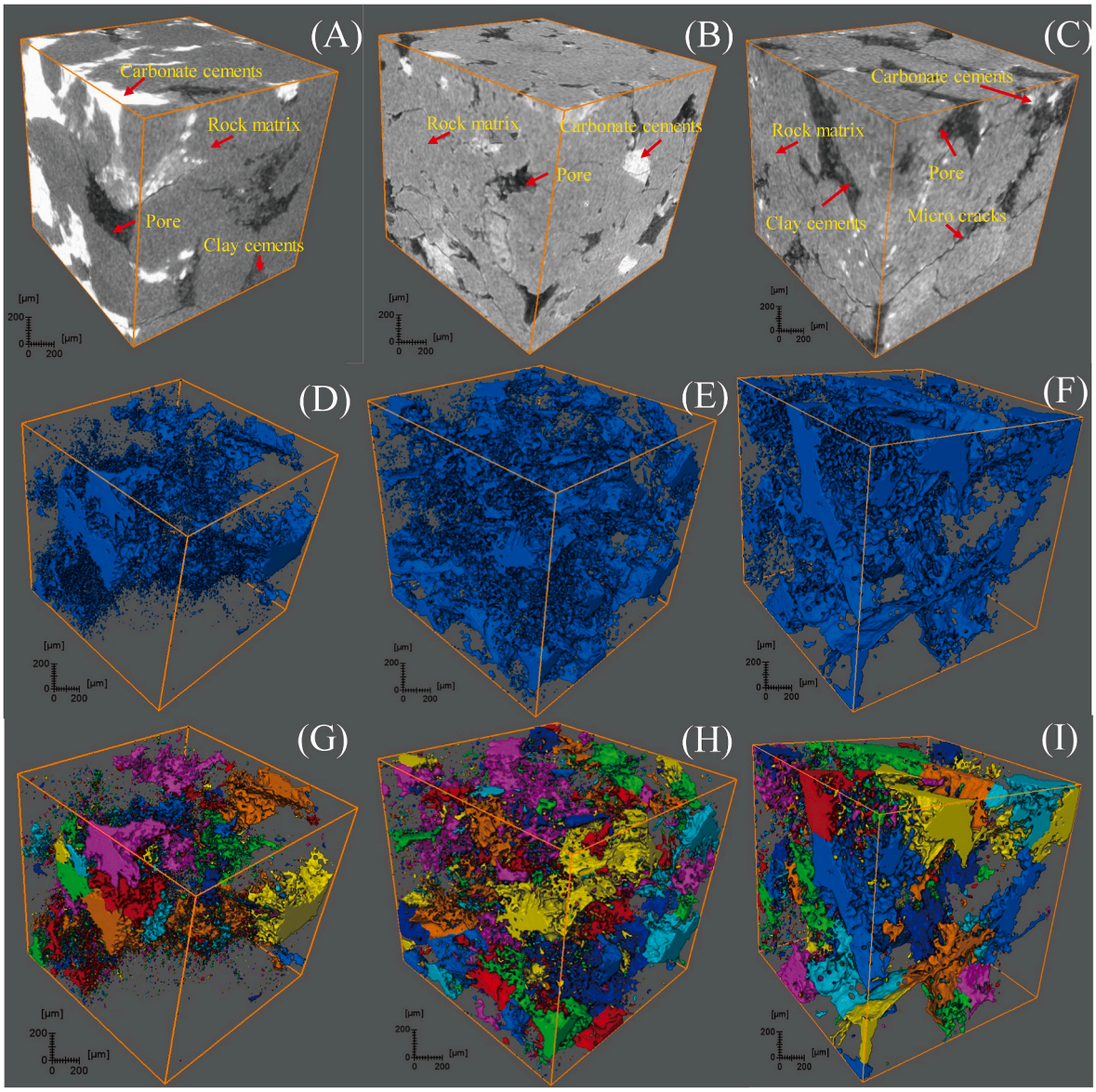

Fig. 4. Reconstructed three dimensional (3D) grayscale images of three representative samples D19-8 (A), D57-6 (B), and D70-12 (C), 3D binary images showing the pore systems extracted from the rock matrix of the samples D19-8 (D), D57-6 (E), and D70-12 (F), and 3D color-labelled images showing the pore connectivity of the samples D19-8 (G), D57-6 (H), and D70-12 (I). (For interpretation of the references to color in this figure legend, the reader is referred to the Web version of this article.)

Table 3
Pore structure parameters derived from X-CT measurement.

Sample	R_{avg}(μm)	R_{50} (μm)	V_{avg}(μm^3)	S_{avg}(μm^2)	C_{adjc}	VF_c	Porosity (%)
D19-8	6.63	182.28	50031.44	3679.26	1.50	0.65	2.18
D69-19	7.06	113.45	37200.64	3588.61	1.87	0.91	1.93
D23-3	7.48	122.42	82985.61	7769.97	1.90	0.91	2.29
D21-1	7.79	196.95	90606.50	8028.96	2.31	0.96	5.06
D9-15	7.70	108.75	25992.49	4168.11	1.89	0.64	3.95
D77-23	9.16	168.09	159192.48	11355.86	2.04	0.94	8.46
D69-20	7.99	136.46	48597.07	4717.06	1.91	0.78	5.17
D23-4	8.11	97.03	36286.92	5188.03	2.09	0.75	7.75
D57-6	9.12	153.03	157064.51	10472.69	2.87	0.97	13.45
D70-12	8.24	95.27	38141.27	4757.46	2.02	0.67	4.09

Note that R_{avg} = average pore radius, R_{50} = pore radius corresponds to the pore with volume fraction of 50% on the cumulative volume fraction curve, V_{avg} = average pore volume, S_{avg} = average surface area, C_{adjc} = average coordination number of connected pores, VF_c = volume fraction of connected pores.

small pores in quantity are responsible for the distinctions between R_{avg} and R_{50} (Table 3). Some slit pores with laminar appearances, believed to be MCs, are identified in the system (Fig. 2C, Figs. 4C, F, I). They are characterized by large surface areas but small pore volume, acting as channels connecting the pores (Fig. 4I).

The structures of the pore systems are varied. The pore system of the sample D57-6 is dominated by superimposed and interconnected large interPs, exhibiting greater bulk pore volumes and better connectivity, and resulting in relative higher porosity and permeability (RHPP) (Fig. 4E, H). For the sample D23-3, the bulk volume and connectivity reduce, and spatial distribution of the pore system becomes more disperse due to the evident increases of the small D-intraPs and tiny interCs in the networks, resulting in ultralow permeability and porosity (UPP) (Fig. 4D, G). However, the situation becomes complex in the sample D70-12, which has a major structure composed of slit MCs and relative small pores (Fig. 4F, I). The pore system is characterized by small bulk pore volume but better connectivity, which is quite different from the connectivity variations of the systems solely controlled by pores. The pore clusters generate from the tiny interCs, small D-intraPs, and laminar MCs reduce the system pore volume, leading to porosity reductions. However, these separated pore clusters are connected by the MCs, which significantly improve the system connectivity and result in abnormal high permeability (Fig. 4I). The petrophysical properties show totally different variations in the pore systems with MCs, which should be noted when applying the permeability estimation models.

The X-CT porosities are shown in Table 3, ranging from 1.93 to 13.95% (avg. 5.43%) and are a little higher than helium porosity since some disconnected pores are detected. The plane porosity distributions obtained from 400 continuous tomography slices of the ten samples are shown in Fig. 5. The fluctuated porosity distributions indicate strong microscopic heterogeneities, with plane porosity spanning in a wide range of 0.11–25.07% and median plane porosity between 4.74 and 19.08% (Fig. 5). For the UPP samples, the amplitudes of the porosity distributions are much lower and distribution patterns tend to be more fluctuated than those with RHPP. However, for the samples D9-15, D69-20, D23-4, and D70-12, the distribution patterns are relative flat and exhibit medium amplitudes in comparison, suggesting porosity heterogeneity reductions induced by the presences of MCs.

The PSDs, the calculated volume fraction distributions of the pore size, are shown in Fig. 6, including the full-range pore radius distribution (FPSD) and disconnected pore radius distribution (DPSD). The DPSDs, exhibiting the volume fraction distributions for the pores with coordination number of zero, are firstly reported (Zeng et al., 2017; Qiao et al., 2019b). Despite of the dominant role of small pores in pore quantity from the observation of CTS and SEM, the volume fraction distributions confirm that the storage spaces of the tight sandstone is dominated by pores with radii >100 μm, followed by pores with radii <50 μm. With increasing permeability, the peaks of the FPSDs become right-skewed, the average and median pore radii rise, and proportions of pores with radii >100 μm increase. However, differences occur in the samples D9-15, D69-20, D23-4, and D70-12, they are characterized by relative narrower size distributions, smaller average and median pore sizes, and higher contents of pores with radii <50 μm (Fig. 6, Table 3).

The amplitude differences (green parts in Fig. 6) between the FPSD and DPSD and amplitudes of DPSD indicate the connected and disconnected proportions of pores with certain radii, respectively. The connected proportions rise with pore radii, indicating that the smaller pores (<50 μm) are partly connected, while larger pores (>100 μm) tend to be fully connected, and the system connectivity is dominated by large pores. However, for the sample D19-8 with ultralow permeability, parts of large pores (>100 μm) are disconnected, which may be attributed to the block of throats resulted from intense compaction and cementation. The connected proportions of the pores with radii <100 μm rise with the permeability and show significant increments in the samples D69-20, D23-4, and D70-12 owing to the presences of MCs (Fig. 6). The ratio of the connected pore volume to total pore volume is proposed to quantify the system connectivity, which spans the range 0.67–0.97 with a mean of 0.82 and shows positive correlation with permeability (Table 3).

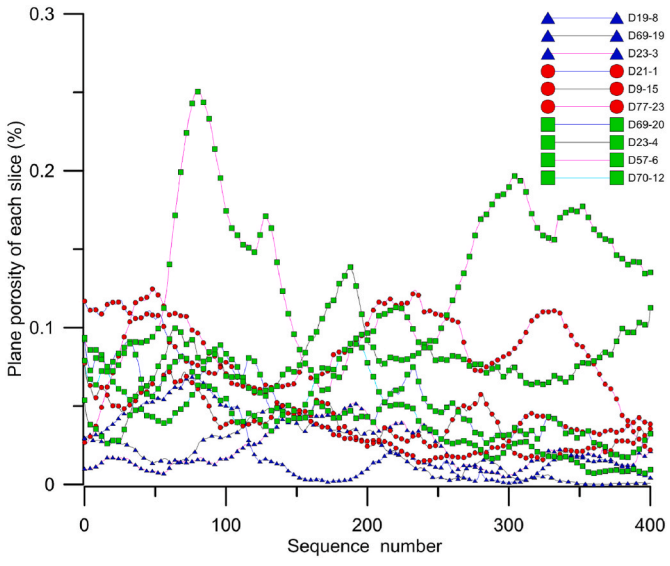

Fig. 5. Plane porosity plots obtained from 400 continuous X-CT tomography images.

4. Discussion

4.1. Pore structure attributes and classifications

4.1.1. Pore structure differences

The pore constitutes show differences among the samples. For the UPP samples, the pore spaces are dominated by the D-intraPs and InterCs, few amounts of D-interPs and barely no P-interPs present (Fig. 2A and D). The situation reverses in the RHPP samples, in which the P-interPs and D-interPs show dominance in porosity, while the D-intraPs and InterCs are volumetrically minor (Fig. 2B and E). The pore constitutes become complicated in the samples with low porosity and high permeability (LPHP), comprising D-interPs, D-intraPs, InterCs, and MCs. The porosity mainly originates from the D-intraPs and InterCs. The MCs contribute little to the porosity but tremendously enhance the pore connections (Fig. 2C and F).

The pore geometrical attributes vary significantly (Table 3), the UPP samples are characterized by left-skewed PSDs with average pore radii (R_{avg}) ranging from 6.63 to 7.48 μm (avg. 7.06 μm) and average median pore radius (R_{50avg}) of 138.38 μm, resulting in small average pore volume (V_{avg}) of 56739.23 μm^3 and small average surface area (S_{avg}) of 5012.61 μm^2 (Fig. 6). The R_{avg}, V_{avg}, and S_{avg} rise with the PSDs shifting to the right on the X-axis in the RHPP samples, which are 8.69 μm, 135621.16 μm^3, and 9952.50 μm^2, respectively. However, this variation rule does not fit for the LPHP samples, which have more fluctuated PSDs than the others (Fig. 6). These samples have medium R_{avg} of 8.01 μm but smaller V_{avg} and S_{avg}, suggesting complete different pore structure constructions. The low values of V/S confirm the presences of MCs, which are responsible for the abnormal permeability variation (Table 3).

The variations in the pore constitutes and geometrical attributes result in connectivity differences (Table 3). The RHPP tight sandstone exhibits the best connectivity with highest average coordination number of connected pores (C_{adjc}) ranging from 2.04 to 2.87 (avg. 2.41) and high connected pore volume fraction (VF_c) between 0.94 and 0.97 with a mean of 0.96, agreed with the dominant role of superimposed and interconnected large pores in the pore volume (Fig. 4H, Table 3). The pore connectivity of the UPP samples reduces evidently owing to the reductions in the pore sizes, volumes, and contents of InterPs, with C_{adjc}

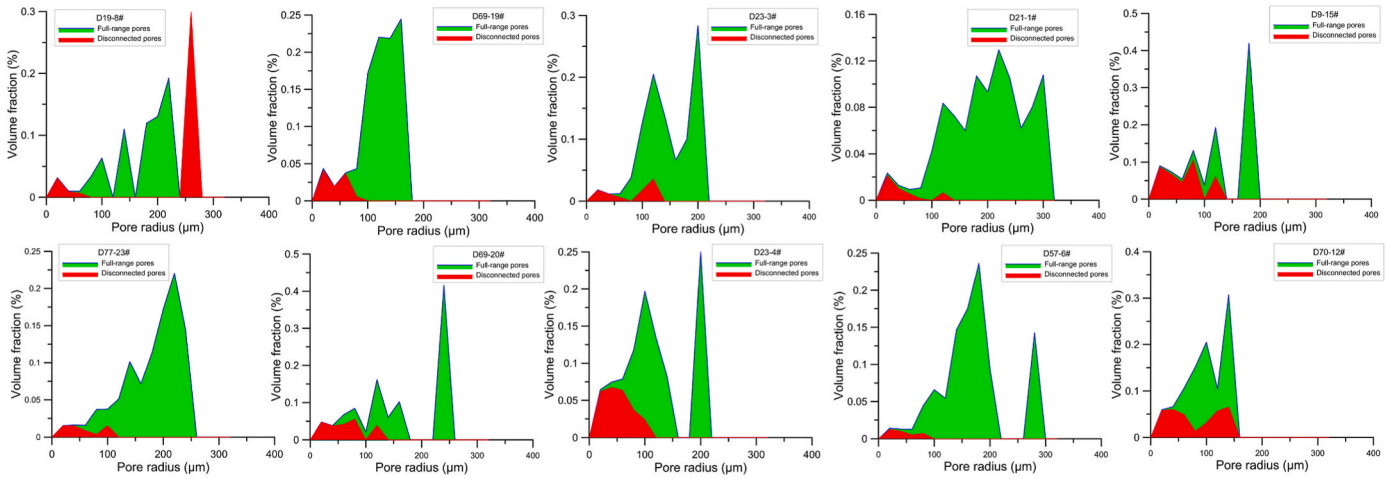

Fig. 6. The full-range pore size distribution (the total of the green and red areas), pore size distribution of disconnected pores (the red area), and pore size distribution of connected pores (the green area) derived by pore network modelling (PNM) conducted on the X-CT measurements. (For interpretation of the references to color in this figure legend, the reader is referred to the Web version of this article.)

and VF_c decreasing to the range 1.50–1.90 (avg. 1.76) and 0.65–0.91 (avg. 0.82), respectively. However, the connectivity of the LPHP samples is different, which is characterized by a high C_{adjc} in the range 1.91–2.09 (avg. 2.01) but low VF_c between 0.67 and 0.78 (avg. 0.73) (Table 3). The reverse variation trends of C_{adjc} and VF_c generate as MCs have great positive impacts on the enhancement of the coordination numbers of the IntraPs and InterCs but limited contributions to the connected volume, suggesting that the MCs exhibit completely different effects on permeability comparing with pores (Fig. 4F and I).

To probe the microscopic heterogeneity, heterogeneity factor and fractal dimension are proposed based on the continuous plane porosity distributions and T_{2c} spectrums, respectively (Figs. 3 and 5). The heterogeneity factor (F_h) describes the variation degree of the plane porosities and can be calculated using Eq. (1). The results indicate variant microscopic heterogeneity of tight sandstone with F_h between 1.22 and 4.62 (avg. 2.24) (Table 4), of which the UPP samples are the most heterogeneous with F_h in the range 2.62–4.62 (avg. 3.44). With increasing permeability, the F_h shows a decreasing tendency, in which the LPHP samples are characterized by low F_h with an average of 1.70, suggesting that the MCs reduce the system heterogeneity.

$$F_h = \frac{\varphi_{\max} - \varphi_{\min}}{\varphi_{med}} \quad (1)$$

where F_h is the heterogeneity factor, $\varphi_{\max}$ is the maximum porosity in plane, %; $\varphi_{\min}$ is the minimum porosity in plane, %; and φ_{med} is the median porosity in plane, %.

As the pore has a fractal nature, the fractal dimension, reflecting the regularity and self-similarity, is generally employed to describe the complicacy and heterogeneity of the pore structure (Mandelbrot, 1975; Mandelbrot et al., 1984; Giri et al., 2012; Xia et al., 2019). The methodology of deriving fractal dimension of the pores in certain size ranges using the NMR data has been thoroughly explained in Appendix A. The results indicate that the microstructure of tight sandstone is dominated by bi-fractal, followed by tri-fractal (Fig. 7, Table 4). The UPP samples are bi-fractal with fractal dimensions of small pores (D_1) ranging from 1.51 to 1.66 (avg. 1.58) and fractal dimensions of large pores (D_3) in the range 2.96–2.99 (avg. 2.97). Similar bi-fractal structure has been discovered in the RHPP samples, which have lower D_1 ranging from 0.66 to 1.60 with 1.13 on average and lower D_3 in the range 2.79–2.92 (avg. 2.88). However, the LPHP samples are tri-fractal, which have low D_1 between 0.58 and 1.23 (avg. 0.99), medium D_3 between 2.92 and 2.97 with a mean of 2.96, and D_2 for the MCs related pores between 2.19 and 2.58 (avg. 2.41). The mean values of the D_1, D_2, and D_3 (D_{avg}) are introduced to further evaluate the system heterogeneity, which span the range 1.79–2.28 and generally exhibit negative trends with permeability. The RHPP samples have a lowest average value of 2.00, while the UPP samples have a highest value of 2.28. However, the LPHP samples have relative homogeneous pore systems with D_{avg} in the range 1.99–2.26 (avg. 2.12), which agree well with the medium F_h value. The results confirm that the way of MCs in influencing the microscopic heterogeneity is also completely different from that of the pores.

Table 4
Heterogeneity factor and pore fractal of ten tight sandstone samples.

Sample	Heterogeneity factor	Pore fractal			
		D_1	D_2	D_3	D_{avg}
D19-8	4.62	1.66	/	2.98	2.32
D69-19	3.07	1.56	/	2.97	2.26
D23-3	2.62	1.51	/	2.99	2.25
D21-1	2.65	1.60	/	2.79	2.20
D9-15	1.63	1.23	2.58	2.97	2.26
D77-23	1.22	1.13	/	2.92	2.03
D69-20	1.60	1.21	2.46	2.97	2.21
D23-4	1.46	0.58	2.42	2.96	1.99
D57-6	1.38	0.66	/	2.92	1.79
D70-12	2.11	0.94	2.19	2.92	2.01

4.1.2. Pore structure classifications

According to the matching responses of pore structures in different measurements, the pore structures of tight sandstone can be classified into three main categories, including the mixed pore type, single-pore dominant type, and dual porous type (Fig. 8). The mixed pore type is common in the UPP samples, e.g. D19-8, D69-19, and D23-3. It is dominated by D-intraPs and InterC in genesis, followed by a few amount of P-interPs and D-interPs (Fig. 2A, Fig 8A), which is characterized by the unimodal T_{2s} distribution pattern with little fluctuations on the long-time domain (Fig. 3A and B), left-skewed PSD with porosity contributions from all sizes of pores (Fig. 6), low V/S of 11.55, and poor connectivity (Table 3, Table 4). The pore system is bi-fractal and intensely heterogeneous with average F_h of 3.43 and D_{avg} of 2.27 (Fig. 7, Table 4). The porosity of single-pore dominant type mainly originates from the P-interPs and D-interPs in origin, resulting in right-skewed bimodal T_{2s} distribution and PSD with predominant porosity contributions from large pores (Fig. 2B, 3D, 6, and 8C). The R_{avg}, V_{avg}, and S_{avg} increase evidently, with greater V/S of 13.43. This type is characterized by better connectivity with greater C_{adjc} of 2.41 and VF_c of 0.96, and more homogeneous bi-fractal structure with lower F_h of 1.75 and D_{avg} of 2.00, which is common in RHPP samples (Fig. 7, Table 3, Table 4). The dual

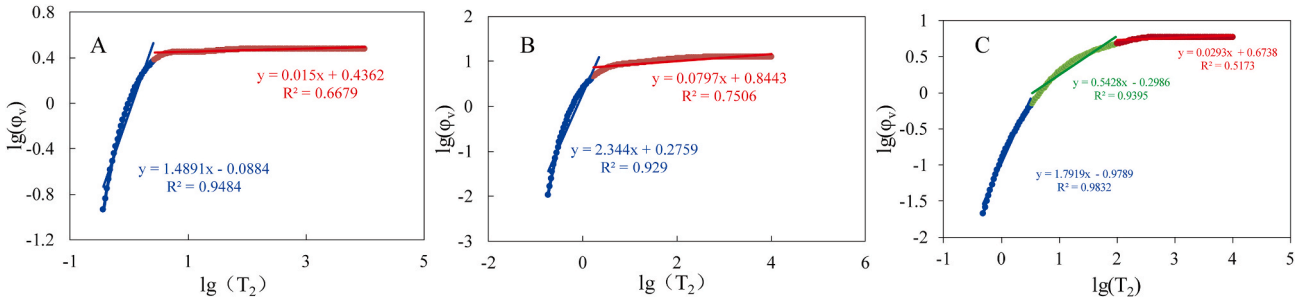

Fig. 7. Fractal structure of the tight sandstone illustrated by three samples D23-3 (A), D77-23 (B), and D69-20 (C).

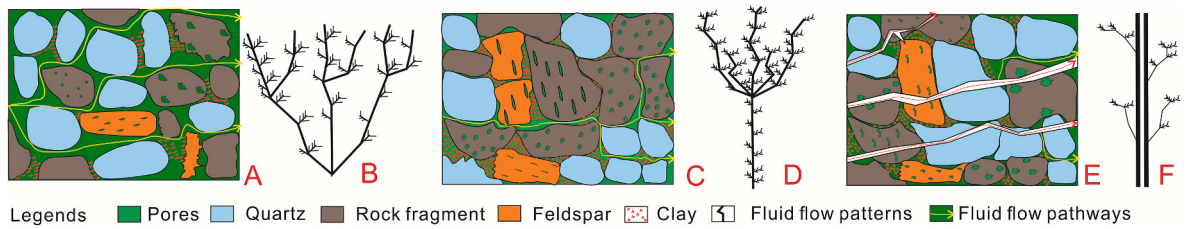

Fig. 8. The sketch maps for the pore structure systems of the single-pore dominant pore structure type (A), mixed pore structure type (C), and dual porous pore structure type (E) and fluid flow inside them. The deduced continuous fluid flow pathways for the single-pore dominant (B), mixed pore (D), and dual porous pore structure types (F).

porous type mainly comprises D-intraPs, InterCs, and MCs in genesis (Figs. 2C, Fig 8E). The dominant roles of D-intraPs and InterCs in porosity and MCs in connections lead to narrower bimodal T_{2s} with smaller amplitude differences between the main and secondary peaks (Fig. 3J), and more fluctuated left-skewed PSD (Fig. 6). The pore system has small R_{avg}, V_{avg}, and S_{avg}, but exhibits an evident reduction in the V/S (avg. 7.89). Its connectivity is better than the mixed pore type but poorer than the single-pore dominant one with C_{adjc} of 2.01, however, the VF_c is low owing to the little contributions of MCs to the connected volume (Table 3, Table 4). Its another remarkable feature is the medium homogenous tri-fractal pore system with low average F_h of 1.70 and D_{avg} of 2.12, exhibiting totally different pores structure variation rules comparing with the bi-fractal pore-controlled types (Fig. 7, Table 4). This type is common in the LPHP samples.

The percolation theory and pore-scale fluid phenomenon publications have reported that a continuous percolation network, formed only if the connected pore volume reaches a certain value, is the basis of the fluid flow through a reservoir (Hunt, 2014; Daigle and Johnson, 2016). Intergranular pores serve as the dominant pathways for the continuous percolation network, followed by intragranular and intercrystalline pores (Xiao et al., 2018; Tian et al., 2020). Situation becomes complicated in tight sandstone. Although the intergranular pores still act as the main pathway, but parts of them can hardly be connected owing to the narrowing of throats. Moreover, the intercrystilline pores contribute more to the percolation network (Lai et al., 2016b; Xiao et al., 2018; Qiao et al., 2020b). Combining percolation theory, tree-like pore network proposed by Sakhaee-Pour and Bryant (2014), and pore structure characterization in our study, the fluid flow pathways of the three types of pore structure are deduced in Fig. 8. In the single-pore dominant one, the well-developed intergranular pores form plenty mainstream pathways that run through the system, while the intragranular and intercrystalline pores form short branches along the main pathways, which are generally ends of the fluid flow (Fig. 8A). The continuous percolation network may exhibit an arbuscular appearance (Fig. 8B). The numbers of mainstream pathways reduce evidently due to the sharp decrease of intergranular spaces in the mixed pore type. Intercrystalline pores become necessary paths for the fluid flow, connecting the adjacent intergranular spaces into short pathways, serving as short branches along the narrowed mainstream lines, forming a floriform shape in plane (Fig. 8C and D). However, the MCs that run through the pore system construct the mainstream pathways in the dual porous structure, taking the place of the intergranular pores (Fig. 8E). The short pathways formed by the combinations of intergranular and intercrystalline pores become branches of the main paths with little contribution to the fluid flow. The network can be described as a tubular structure (Fig. 8F). Obviously, the floriform and arbuscular percolation pathways share similar reticular flow systems as pores control the percolation (Fig. 8B and D), and therefore the permeability variation should follow the changing rules of the pores. However, the tubular network exhibits completely different pipe-like percolation, indicating different permeability variation mechanisms (Fig. 8F).

4.2. *Effects of pore structure on the permeability*

It's no doubt that the changes in the pore structure attributes are dominantly responsible for the complex permeability variations in tight sandstone. Correlation analyses between the key parameters of pore size, connectivity, fluid mobility, heterogeneity, and permeability are conducted to investigate the effects of pore structure on permeability.

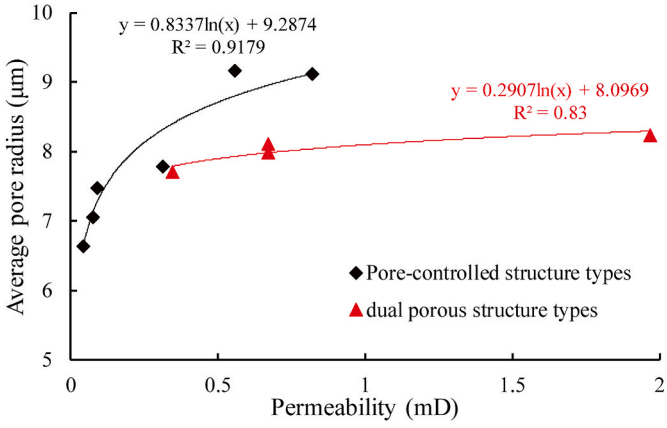

Fig. 9. Correlations between permeability and average pore radii in the pore-controlled and dual porous tight sandstone.

Poor correlations are identified when analyses cover all of the samples, suggesting that the permeability is not solely determined by the pore attributes or fluid mobility of the pore system (Fig. 9). Considering the different variation rules of pore structure attributes and permeability in different structure types, the analyses are separately conducted on the samples with pore-controlled structure and with dual porous one (Fig. 9). The results suggest that the pore size, connectivity, fluid mobility, and heterogeneity exhibit different effects on the permeability in the pore-controlled and dual porous structures (Figs. 9–12). The permeability of the pore-controlled samples is positively correlated with attributes dominated by the pores, i.e. the average pore radii (Fig. 9), VF_c (Fig. 10A), C_{adjc} (Fig. 10B), movable porosities (Fig. 11A), FFI/BVI (Fig. 11B), and S_{mw}/S_{iw} (Fig. 11C), indicating that greater pore size, higher fluid mobility, and better connectivity are favorable for the permeability enhancement of the pore-controlled tight sandstone. Negative correlations between F_h, D_{avg}, and permeability (Figs. 12A and B) suggest that higher structural heterogeneity will result in permeability loss. However, the condition turns complicated in the dual porous tight sandstone, there are no obvious correlations between the permeability and parameters mainly determined by pores (Figs. 9–12), implying that pores have little contribution to the permeability. The strong negative correlations between permeability, D_2, and D_{avg} that are closely associated with the MCs suggest the dominant control of features of MCs on the permeability of dual porous tight sandstone (Fig. 12B and C). However, the controlling mechanisms of MCs on permeability remain to be investigated. As far as the effects of pore structures on the permeability are concerned, the permeability estimation models should be modified under constrain of pore structures before they are employed, in which the pore structure types should be firstly considered, followed by pore connectivity.

4.3. Predicting permeability under the constrain of pore structure

In this study, three permeability estimation models are invoked, of which the Coates and SDR models are applied on the basis of NMR and X-CT results, while the Pittman model is employed based on the PSDs derived from X-CT. It has been indicated that these models should be modified before they are employed because the pore structure exerts complex influences on the permeability of tight sandstone. As indicated, the modification should taking the pore structure types and key pore structure parameters used in the models into account. In this paper, the applicability of the original models, models with key parameters calibrated, and models with parameters calibrated and structural types considered is examined using the MLR method that can determine the empirical relationships between the permeability, porosity and key pore structure attributes (Purcell, 1949; Pittman, 1992; Rezaee et al., 2012).

4.3.1. The Coates model

In the original Coates model, the permeability is estimated by Eq. (2) in the following: (Coates et al., 1999; Rezaee et al., 2012).

$$K = \left[\left(\frac{\varphi}{C}\right)^2 \left(\frac{FFI}{BVI}\right)\right]^2 \tag{2}$$

where K is permeability, mD; φ is the porosity, %; C is the constant, which varies in different study areas; FFI is the free fluid index; BVI is the bound volume of irreducible water. When taking logarithm on both sides of Eq. (2), it can be expressed as follow:

$$\lg K = C_1 + \alpha \lg \varphi + \beta \lg \frac{FFI}{BVI} \tag{3}$$

where C_1, α, and β are the constants.

The porosity φ and fluid mobility index $\frac{FFI}{BVI}$ determine the estimation accuracy, which are generally acquired from NMR porosity and ratio of movable to irreducible water saturation identified by the $T_{2cutoffs}$, respectively. As the NMR porosity exhibits a deviation from helium porosity due to the clay bound water or capillary bound water remaining in the fibrous or laminar structures of the clay minerals (Clarkson et al., 2012; Xiao et al., 2017a) and pore connectivity strongly influences the permeability (Cai et al., 2014; Ghanbarian et al., 2019), the porosity φ used should be modified taking the helium porosity and pore connectivity into account. Moreover, the FFI/BVI is somehow inappropriate in describing the fluid mobility due to the underestimation of movable capillary bound water existing in the tiny pores with sizes less than the $T_{2cutoffs}$ and immovable clay bound water in the large pores with sizes greater than the $T_{2cutoffs}$ (Dai et al., 2016; Lai et al., 2018; Huang et al., 2018; Qiao et al., 2020d). These movable capillary bound water and immovable clay bound water separately fall into the weakly bound water layer and strongly bound water layer according the clay bound water distribution model (Woodruff and Revil, 2011; Li et al., 2019; Yang and Yu, 2020) based on the DLVO theory (Tuller and Or, 2003; Lebeau and Konrad, 2010; Israelachvili, 2011), they are highlighted by the clay bound water concept in the condition that the capillary bound water could not be fully centrifuged (Lonnes et al., 2003; Martin and Dacy, 2004), and should not be neglected in the fluid mobility evaluation of tight sandstone. Huang et al. (2018) and Qiao et al. (2020c, 2020d) have reported that a more proper S_{mw}/S_{iw} can be obtained in tight sandstone using the clay bound water concept than employing the common bound water constraint model, which can be supported by the Lai et al. (2018b). Therefore, the porosity and FFI/BVI are replaced by the connected effective porosity φ_c that is calculated by multiplying the VF_c and helium porosity, and S_{mw}/S_{iw}, respectively, the modified equation is shown as follow:

$$\lg K = C_1 + \alpha \lg \varphi_c + \beta \lg \frac{S_{mw}}{S_{iw}} \tag{4}$$

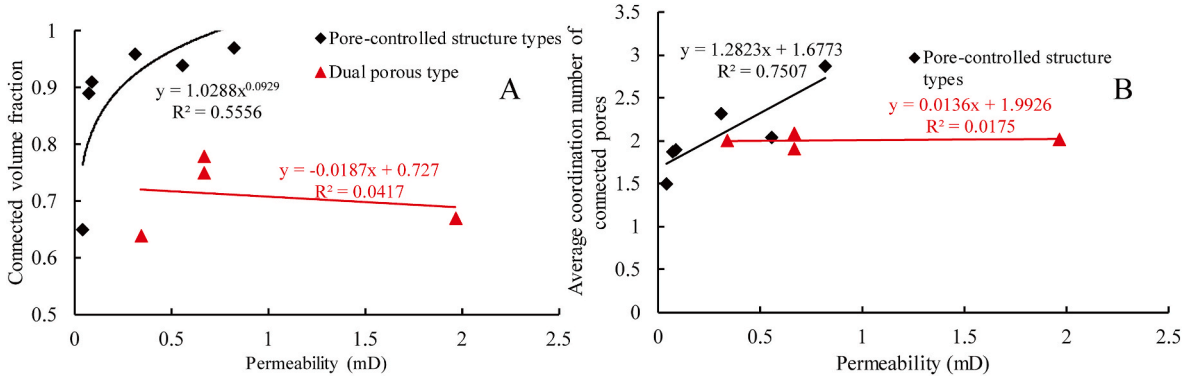

Fig. 10. Effects of pore connectivity on the permeability. Correlations between permeability and volume fraction of connected pores (A) and relationships between average coordination number of connected pores and permeability (B) in the pore-controlled and dual porous tight sandstone.

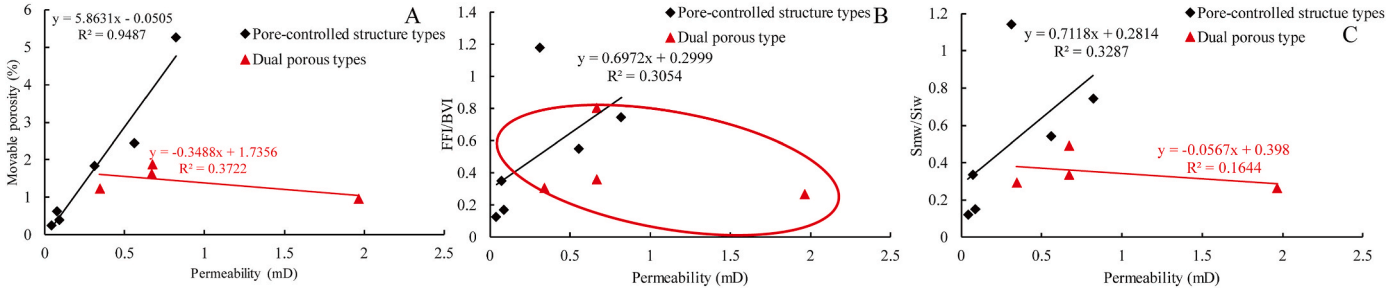

Fig. 11. Impacts of fluid mobility on the permeability. Correlations between permeability and movable porosity (A), FFI/BVI (B), S_{mw}/S_{iw} (C) in the pore-controlled and dual porous tight sandstone.

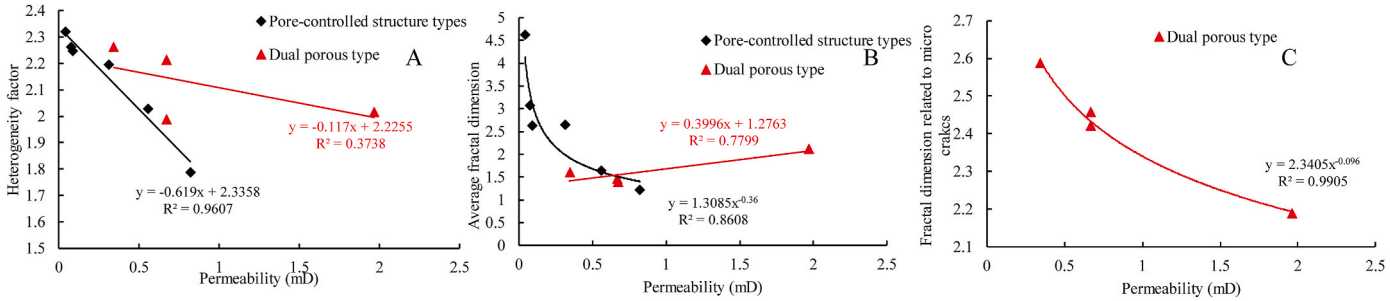

Fig. 12. Influences of microscopic heterogeneity on the permeability. Correlations between permeability and heterogeneity factor (A), average fractal dimension (B), fractal dimensions related to the micro cracks (C) in the pore-controlled and dual porous tight sandstone.

where φ_c is the connected effective porosity, %; S_{mw}/S_{iw} is the ratio of movable water saturation to irreducible water saturation.

As far as the impacts of pore structure on permeability are concerned, the MLR analyses, the most reliable method to determine the empirical relationships between permeability, porosity, and other petrophysical parameters, are conducted on the original Coates model, modified Coates model, and two models considering the structural types (i.e. excluding the samples with dual porous structure) to determine the empirical constants in these models and to examine their performances. The regression equations with constants determined for the four models are listed in Table 5. The results suggest that the modified Coates model is more accurate owing to the appropriate consideration of pore structure, especially the connectivity, which has much higher R^2 and R_{adj}^2 than the original one. Notably, evident increases have been discovered in the regression analyses of the two models when the dual porous samples are excluded, of which the equation derived from original Coates model has R^2 greater than 0.97 and R_{adj}^2 greater than 0.94, while that obtained from the modified model shows greater values of 0.99 and 0.98 (Table 5). These results indicate that the pore structure type should be primarily considered in the permeability estimation of tight sandstone because the controlling mechanisms of dual porous structure on permeability are distinct from those of pore-controlled types, followed by pore connectivity. The calibrated Coates model perfectly improves the permeability prediction accuracy of pore-controlled tight sandstone.

Table 5
Empirical equations derived from the original and modified Coates and SDR models.

Model	Equations	R^2/R_{adj}^2
Original Coates model	$lgK = -1.607 + 1.717lg\varphi + 0.153lgFFI/BVI$	0.615/ 0.487
Modified Coates model	$lgK = -1.344 + 1.366lg\varphi_c - 0.359lgS_{mw}/S_{iw}$	0.641/ 0.521
Original Coates model excluding the dual porous samples	$lgK = -1.395 + 1.346\ lg\varphi + 0.483\ lgFFI/BVI$	0.972/ 0.945
Modified Coates model excluding the dual porous samples	$lgK = -1.215 + 1.064lg\varphi_c + 0.042lgS_{mw}/S_{iw}$	0.992/ 0.984
Original SDR model	$lgK = -1.944 + 0.486lgT_{2gm} + 1.595lg\varphi$	0.746/ 0.674
Modified SDR model	$lgK = -1.265 + 1.010lgT_{2gm} + 0.356lg\varphi_c$	0.712/ 0.629
Original SDR model excluding the dual porous samples	$lgK = -1.965 + 0.402lgT_{2gm} + 1.538lg\varphi$	0.980/ 0.967
Modified SDR model excluding the dual porous samples	$lgK = -1.437 + 0.232lgT_{2gm} + 1.099lg\varphi_c$	0.997/ 0.995

4.3.2. The SDR model

The SDR model is generally expressed as: (Rezaee et al., 2012; Xiao et al., 2017a).

$$K = aT_{2gm}{}^2\varphi^4 \quad (5)$$

where T_{2gm} is the geometric mean of T_2 distribution, ms; φ is the NMR porosity, %; a is generally equal to 4 in sandstone, which is determined by the calibration with porosity and permeability. Taking logarithm on both sides of the equation, it could be expressed as follow:

$$K = C_2 + \alpha lg\varphi + \beta lgT_{2gm} \quad (6)$$

where C_2, α, and β are constants, which are commonly determined by the reservoirs investigated.

In the SDR model, the porosity is the only concern in the estimation, which can be calibrated employing the φ_c used in the modified Coates model. MLR is conducted on the original SDR model, modified SDR model, and the two models excluding the dual porous samples to determine the constants in these models and to examine their performances. The little differences in the R^2 and R_{adj}^2 between the original and modified SDR models suggest that the porosity exerts little impacts on the permeability estimation (Table 5). The two coefficients rise sharply when the dual porous samples are excluded in regressions, indicating the primary control of pore structure type on the permeability. Additionally, the slightly higher coefficients of the modified model ($R^2 = 0.998$ and $R_{adj}^2 = 0.996$) than the original one suggest positive effects of pore connectivity on the permeability in pore-controlled tight sandstone (Table 5).

4.3.3. The Pittman model

The PSD has been widely used in the permeability estimation since Windland developed the empirical relationships between the permeability, porosity, and pore-throat size (Kolodzie Jr, 1980), which has been further extended by Pittman using the regression equation yielding best R^2 for permeability, porosity, and pore size (Pittman, 1992). The Pittman model has been accepted in the tight sandstone, whereby many empirical models have been proposed, all of which can be described as follow:

$$\lg K = C + \lg\varphi + \lg r_i \quad (7)$$

where $C$is the empirical constant, φ is the helium porosity, %, and r_i is the pore radius corresponding to a certain cumulative mercury saturation or cumulative volume fraction, μm.

The Pitman model and its MLR method can be performed on the PSDs obtained from the X-CT as the cumulative volume fraction and cumulative mercury saturation can be regarded as the same in principle. The porosity and r_i are two concerns in determining the applicability of the model. The porosity in the Pittman model can be replaced by the φ_c as indicated. Taking the effects of pore connectivity into accounts, the r_i is replaced by the r_{ic} obtained from the connected pore size distribution (CPSD) that is acquired by the combination of FPSD and DPSD. The modified model can be expressed as:

$$\lg K = C + \lg\varphi_c + \lg r_{ic} \quad (8)$$

where φ_c is the connected effective porosity, %; r_{ic} is the pore radius corresponding to a certain cumulative volume fraction on the CPSD, μm.

The MLR analyses are performed on the original Pittman model, modified Pittman model, and two models considering the structural types within the volume fraction range of 5–50% with an interval of 5% to determine the constants of theses models and to check their accuracies. The regression equations and their determination coefficients are listed in Tables 6 and 7. The relative high determination coefficients suggest a good applicability of Pittman model on the basis of the PSDs from X-CT and the r_{35} yields the best correlation with the porosity and permeability in original model. Higher coefficients of the majority of the equations obtained from the modified model indicate that the modified one taking the pore connectivity into account is more appropriate in the prediction, of which the r_{25} yields best correlation (Table 6). Similar sharp increases have been also discovered when the two models are applied to the data excluding the dual porous sandstone, confirming that the pore structure types dominate the applicability of the permeability estimation (Table 7). The results suggest that the r_{25} and r_{10} yield best correlations with porosity and permeability in the original and modified Pittman models considering structural types, respectively. Great determination coefficients greater than 0.97 between r_{10} and permeability suggest the strong estimation reliability of the modified Pittman model that has taken pore structure type into consideration (Tables 6 and 7).

Table 6
Empirical equations developed from regression analysis performed on the original and modified Pittman models.

Equation-OP	R^2/R_{adj}^2	Equations-MP	R^2/R_{adj}^2
$\lg K = -0.447 + 1.145\lg\varphi - 0.400\lg r_5$	0.685/ 0.595	$\lg K = 3.696 + 1.137\lg\varphi_c - 2.587\lg r_5$	0.754/ 0.672
$\lg K = 0.007 + 1.128\lg\varphi - 0.605\lg r_{10}$	0.707/ 0.623	$\lg K = 2.306 + 1.164\lg\varphi_c - 1.747\lg r_{10}$	0.719/ 0.639
$\lg K = 0.139 + 1.149\lg\varphi - 0.648\lg r_{15}$	0.687/ 0.597	$\lg K = 2.819 + 1.141\lg\varphi_c - 1.957\lg r_{15}$	0.716/ 0.634
$\lg K = 0.496 + 1.149\lg\varphi - 0.648\lg r_{20}$	0.691/ 0.602	$\lg K = 3.700 + 1.053\lg\varphi_c - 2.325\lg r_{20}$	0.629/ 0.481
$\lg K = 1.012 + 1.113\lg\varphi - 1.031\lg r_{25}$	0.698/ 0.612	$\lg K = 3.989 + 0.946\lg\varphi_c - 2.428\lg r_{25}$	0.776/ 0.686
$\lg K = 1.022 + 1.083\lg\varphi - 1.012\lg r_{30}$	0.545/ 0.393	$\lg K = 2.629 + 1.015\lg\varphi_c - 1.733\lg r_{30}$	0.700/ 0.580
$\lg K = 1.888 + 1.004\lg\varphi - 1.419\lg r_{35}$	0.752/ 0.669	$\lg K = 3.635 + 0.962\lg\varphi_c - 2.211\lg r_{35}$	0.731/ 0.624
$\lg K = 1.141 + 1.07 3\lg\varphi - 1.037\lg r_{40}$	0.528/ 0.370	$\lg K = 1.459 + 0.727\lg\varphi_c - 1.047\lg r_{40}$	0.340/ 0.011
$\lg K = 0.599 + 1.060 \lg\varphi - 0.761\lg r_{45}$	0.496/ 0.328	$\lg K = 3.186 + 0.952 \lg\varphi_c - 1.961\lg r_{45}$	0.629/ 0.444
$\lg K = 2.017 + 1.016 \lg\varphi - 1.438\lg r_{50}$	0.719/ 0.626	$\lg K = 1.812 + 0.995 \lg\varphi_c - 1.285\lg r_{50}$	0.659/ 0.522

Note that Equation-OP and Equations-MP are the regression equations derived from original Pittman model and modified Pittman model, respectively.

Table 7
Empirical equations developed from regression analysis performed on the original and modified Pittman models excluding the samples with dual porous structure.

Equations-OPE	R^2/ R_{adj}^2	Equations -MPE	R^2/ R_{adj}^2
$\lg K = -1.289 + 1.907\lg\varphi + 0.045\lg r_5$	0.966/ 0.944	$\lg K = -3.009 + 1.081\lg\varphi_c + 0.958\lg r_5$	0.978/ 0.964
$\lg K = -1.674 + 1.905\lg\varphi + 0.246\lg r_{10}$	0.969/ 0.949	$\lg K = -3.779 + 1.089\lg\varphi_c + 1.309\lg r_{10}$	0.979/ 0.965
$\lg K = -1.863 + 1.090\lg\varphi + 0.366\lg r_{15}$	0.970/ 0.951	$\lg K = -2.984 + 1.095\lg\varphi_c + 0.8841.957\lg r_{15}$	0.973/ 0.954
$\lg K = -1.952 + 1.107\lg\varphi + 0.365\lg r_{20}$	0.971/ 0.951	$\lg K = -2.502 + 1.105\lg\varphi_c + 0.626\lg r_{20}$	0.952/ 0.904
$\lg K = -2.238 + 1.104\lg\varphi + 0.496\lg r_{25}$	0.973/ 0.954	$\lg K = -2.628 + 1.116\lg\varphi_c + 0.676\lg r_{25}$	0.974/ 0.957
$\lg K = 4.722 + 1.402\lg\varphi - 2.889\lg r_{30}$	0.750/ 0.500	$\lg K = -2.619 + 1.099\lg\varphi_c + 0.669\lg r_{30}$	0.973/ 0.947
$\lg K = -2.262 + 1.278\lg\varphi + 0.489\lg r_{35}$	0.972/ 0.953	$\lg K = -2.592 + 1.099\lg\varphi_c + 0.652\lg r_{35}$	0.973/ 0.945
$\lg K = -2.709 + 1.079 3\lg\varphi + 0.713\lg r_{40}$	0.967/ 0.931	$\lg K = -2.582 + 1.071\lg\varphi_c + 0.655\lg r_{40}$	0.943/ 0.829
$\lg K = -2.475 + 1.078 \lg\varphi + 0.599\lg r_{45}$	0.963/ 0.925	$\lg K = -2.511 + 1.127 \lg\varphi_c + 0.591\lg r_{45}$	0.959/ 0.919
$\lg K = -2.408 + 1.127 \lg\varphi + 0.545\lg r_{50}$	0.976/ 0.961	$\lg K = -2.445 + 1.113 \lg\varphi_c + 0.564\lg r_{50}$	0.973/ 0.946

Note that Equations-OPE and Equations -MPE are the regression equations derived from original Pittman model excluding the samples with dual porous structure and modified Pittman model excluding the samples with dual porous structure, respectively.

4.4. Performance check

To examine the performances of these estimation models indicated above, the permeability is separately calculated using the equations obtained from the original and modified Coates model, SDR model, Pittman model (equations with highest regression coefficients), and all of these models excluding dual porous samples. The correlations of

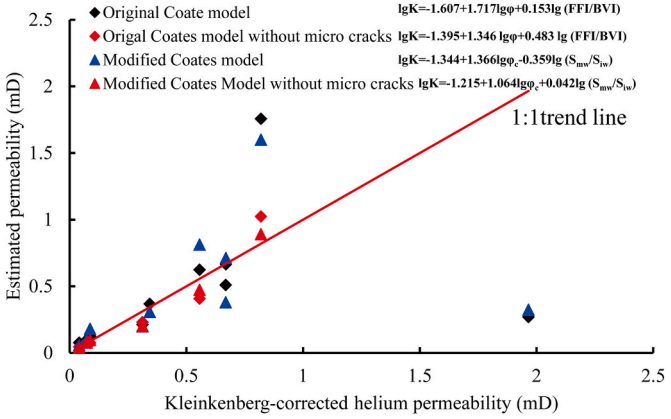

Fig. 13. Plots displaying the relationships between the measured permeability and permeability estimated by the equations obtained from original Coates model, modified Coates model, and the two models excluding the dual porous samples.

estimated permeability and absolute helium permeability are plotted together with 1:1 trend line that describes the perfect match between the estimated and measured values in order to determine the estimation accuracies of these models (Zhao et al., 2015; Wu et al., 2017) (Figs. 13–15). In the Coates model, the permeability estimated by modified model gets closer to the trend line than the original one no matter whether the pore structure types are taken into account, suggesting performances improvement from the consideration of pore connectivity (Fig. 13). However, the evident permeability deviations of the dual porous samples, e.g. D69-20 and D70-12, in the models covering all of the samples, and little differences between the measured and estimated values in the modified Coates model excluding the dual porous samples confirm the primary control of the pore structure types on the changing rule of permeability, which should be addressed in priority. Besides, the reverse of the coefficient values before lg (S_{mw}/S_{iw}) from negative to positive in the two modified models strongly support this results. The situation is quite similar in the performance check of the SDR model (Fig. 14), the modified SDR model considering the pore types provides the most reliable prediction. Predication accuracy losses are indicated by the greater deviations between the estimated and factual permeability in the Pittman model (Fig. 15). However, the modified Pittman model excluding the dual porous tight sandstone is still more appropriate than the others, supporting that the decisive effects of pore structure types and connectivity on the adaptability of Pittman evaluation. This results can also be supported by the coefficient reverse before lg r_{ic} from the modified model to the modified one excluding dual porous samples.

Comparing the performances of these models, the modified Pittman model is adaptive in the estimation of tight sandstone with detail PSD information, while the modified Coates and SDR models are adaptive in the tight sandstone with detail fluid mobility information. It can be also inferred that the modified Coates and SDR models are more reliable than the modified Pittman model in the permeability estimation of tight sandstone, which may probably attributed to the accuracy of CPSD that is limited by the resolution of the X-CT measurement (Qiao et al., 2020a).

In a word, the adaptabilities of all of the modified models strongly depend on the deep understandings of the pore structure of tight sandstone, of which the pore structure types come first, then the pore connectivity follows. The modifications from pore structure characterization provide better understandings for the effects of pore structures on the permeability and perfect estimation models for the pore-controlled tight sandstone. Moreover, the different variation mechanisms of permeability in dual porous tight sandstone remind us that new approaches should be proposed to estimate the tight sandstone with presences of MCs.

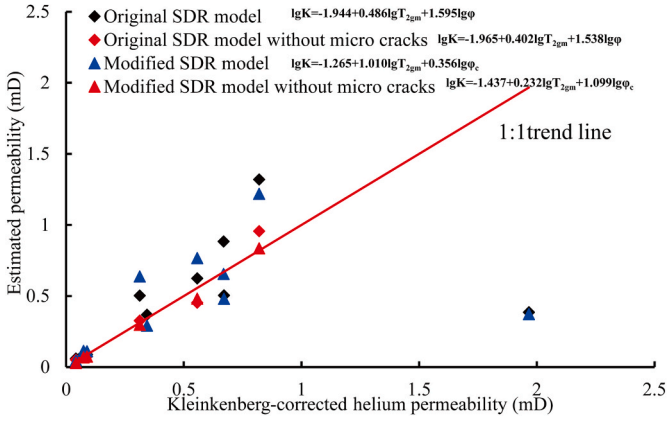

Fig. 14. Plots displaying the relationships between the measured permeability and permeability estimated by the equations acquired from original SDR model, modified SDR model, and the two models excluding the dual porous samples.

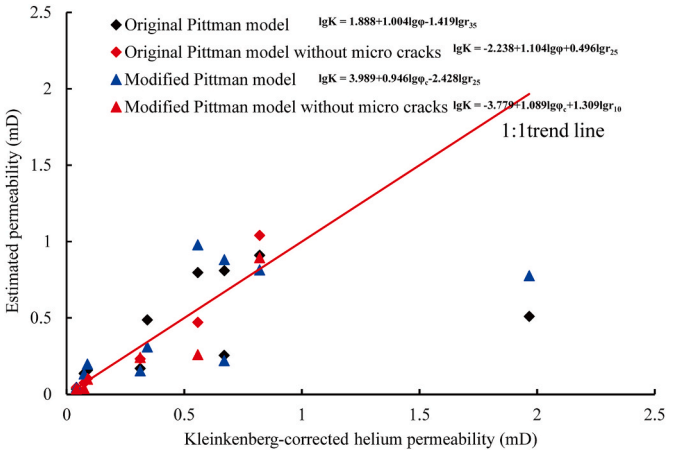

Fig. 15. Plots displaying the relationships between the measured permeability and permeability estimated by the equations with highest regression coefficients obtained from original Pittman model, modified Pittman model, and the two models excluding the dual porous samples.

5. Conclusions

In this paper, three popular permeability estimation models for tight sandstone are calibrated properly on the basis of the systematic pore structure characterization, which integrates CTS, SEM, NMR, and X-CT techniques and incorporates fractal and percolation theory. The main objects of this study are to investigate the impacts of pore structure on permeability and to provide reliable permeability estimation models for tight sandstone. The conclusions can be drawn as follow.

The mixed pore type, single-pore dominant type, and dual porous type are identified in the systematic pore structure characterization of tight sandstone. Differences in the pore genesis and constitutes result in the significant variations in the pore attributes, connectivity, and heterogeneities of the three pore structure types. Especially, distinct variation rules of structural attribute are discovered in the bi-fractal pore-controlled structures (i.e. the mixed pore and single-pore dominant types) and tri-fractal dual porous structure due to the presences of micro cracks.

Pore structure attribute differences result in the distinctions in the continuous fluid percolation pathways. The pore-controlled sandstone shares similar reticular networks controlled by pores, while the dual porous sandstone exhibits a completely different tubular network determined by micro cracks, leading to different permeability variation mechanisms between the two structures. The different correlation trends between the pore structure attributes, fluid mobility, and permeability in the pore-controlled and dual porous structures support the percolation deductions and indicate that the permeability is primarily controlled by the pore structure types. The permeability of pore-controlled tight sandstone is determined by the size, connectivity, and fluid mobility of pores, and affected by pore heterogeneity, while that of dual porous sandstone is determined by the features related to micro cracks.

The Coates, SDR, and Pittman models are firstly modified with consideration of the effects of pore structure on permeability, especially the connectivity and fluid mobility. They are further improved by taking the pore structure types into account. Sharp performance enhancements of the further improved models in the pore-controlled tight sandstone confirm that pore structure types should be firstly addressed, and then pore connectivity follows, in the permeability estimation of tight sandstone. The adaptabilities of the permeability estimation models strongly rely on the understandings of the pore structure of tight sandstone. Moreover, it reminds the geologists of new approaches should be proposed to estimate the dual porous tight sandstone.

This paper provides a comprehensive perspective for the

permeability estimation of the tight sandstone by throwing a deeper light on the effects of pore structure on the permeability. The improved approaches are of vital importance for the reserve prediction, evaluation, and development of the unconventional hydrocarbon, geothermal, and groundwater resources.

Declaration of competing interest

The authors declare that they have no known competing financial interests or personal relationships that could have appeared to influence the work reported in this paper.

Acknowledgements

This study is supported by the National Natural Science Foundation of China (Grant No. 41330319, No. 42130803, and No. 42072174), Foundation of China University of Petroleum Beijing (Grant No. 2462020XKBH016), and fellowship of China Postdoctoral Science Foundation (Grant No. 2020M680030). We sincerely appreciate all anonymous reviewers and the handling editor for their comments and suggestions.

Appendix

A. Calculation of Pore fractal dimension based on the NMR data.

According to the fractal principle, the correlation between the number of pores and pore radius can be described by Eq. (1).

$$N_r = \int_r^{r_{max}} P(r)dr = \alpha r^{-D} \tag{A1}$$

where N_r is the quantity of the pores with radii greater than r, $P(r)$ is the density function of pore radius, r is the pore radius, D is the fractal dimension, α is the proportional constant.

To calculate the derivative of Eq. (1) with respect to r, the $P(r)$ can be expressed using the following Eq. (2).

$$P(r) = \beta r^{-D-1} \tag{A2}$$

where β equals to $-D\alpha$. Therefore, the total volume of pores with radii less than r could be derived by substituting Eq. (2) to Eq. (1).

$$V_r = \int_{r_{min}}^{r} P(r)Fr^3dr = C\left(r^{3-D} - r_{min}^{3-D}\right) \tag{A3}$$

where C is the proportional constant, equaling to $-D\alpha/(2-D)$. V_r is the cumulative pore volume of the pores with radii less than r, μm^3. F is the shape factor, which is 1 when the pore is cubic and is $4\pi/3$ when the pore is sphere, r_{min} is the minimum pore radii, μm. According to Eq. (3), the total volume can be obtained in Eq. (4).

$$V_t = C\left(r_{max}^{3-D} - r_{min}^{3-D}\right) \tag{A4}$$

where V_t is the total volume of the samples, r_{max} is the maximum pore radii. The volume fraction of pore with radii less than r can be expressed as following.

$$S_V = \frac{V_r}{V_t} = \frac{r^{3-D} - r_{min}^{3-D}}{r_{max}^{3-D} - r_{min}^{3-D}} \tag{A5}$$

where S_V is the volume fraction of the pores with radii less than r. As r_{min} is commonly far less than r_{max}, the equation can be simplified as following.

$$S_V = \frac{r^{3-D}}{r_{max}^{3-D}} \tag{A6}$$

On the basis of the correlation between T_2 and pore radius (described by Eq. (7)) (Arns et al., 2005), Eq. (6) can be converted to Eq. (8), and Eq. (8) can be transformed to Eq. (9) by taking double logarithms.

$$\frac{1}{T_2} = \rho\frac{S}{V} = F_s\frac{\rho}{r} \tag{A7}$$

where T_2 is the relaxation time, ms, ρ is the surface relaxitivity. F_s is the shape factor, which equals to 2 for cylindrical pores and equals to 3 for spherical pores. $\frac{S}{V}$ is the ratio of surface area to volume for pores with certain radii.

$$S_V = \left(\frac{T_r}{T_{2max}}\right)^{3-D} \tag{A8}$$

$$\lg S_V = (3-D)\lg T_r - (3-D)\lg T_{2max} \tag{A9}$$

where T_r is the relaxation time of pores with radii less than r, ms, T_{2max} is the maximum relaxation time of the samples, ms. Accordingly, the fractal dimension D for certain kinds of pores can be derived from the slope k of the linear segments on the plots of $\lg S_V$ and log (T_2) ($D = 3 - k$).

As S_V can be expressed as follow:

$$S_V = \frac{\varphi_V}{\varphi_t} \tag{A10}$$

where φ_V is the cumulative porosity of pores with radii less than r, %; φ_t is the total porosity, %. Eq. (9) can be transformed to Eq. (11) in the following.

$$\lg\varphi_V = (3 - D)\lg T_r - (3 - D)\lg T_{2max} + \lambda \tag{A11}$$

where λ is a constant equaling to $\lg\varphi_t$.

References

Adler, P., Jacquin, C.G., Quiblier, J., 1990. Flow in simulated porous media. Int. J. Multiphas. Flow 16 (4), 691–712.

Al Hinai, A., Rezaee, R., Esteban, L., Labani, M., 2014. Comparisons of pore size distribution: a case from the Western Australian gas shale formations. J. Unconventional Oil Gas Resour. 8, 1–13.

Arns, C.H., Knackstedt, M.A., Pinczewski, M.V., Lindquist, W., 2001. Accurate estimation of transport properties from microtomographic images. Geophys. Res. Lett. 28 (17), 3361–3364.

Arns, C.H., Knackstedt, M.A., Pinczewski, W.V., Martys, N.S., 2004. Virtual permeametry on microtomographic images. J. Petrol. Sci. Eng. 45 (1–2), 41–46.

Arns, C.H., Knackstedt, M.A., Martys, N.S., 2005. Cross-property correlations and permeability estimation in sandstone. Phys. Rev. E. 72 (4), 046304.

Banavar, J.R., Schwartz, L.M., 1987. Magnetic resonance as a probe of permeability in porous media. Phys. Rev. Lett. 58 (14), 1411–1414.

Blunt, M.J., Bijeljic, B., Dong, H., Gharbi, O., Iglauer, S., Mostaghimi, P., Paluszny, A., Pentland, C., 2013. Pore-scale imaging and modelling. Adv. Water Resour. 51, 197–216.

Bourbie, T., Zinszner, B., 1985. Hydraulic and acoustic properties as a function of porosity in Fontainebleau sandstone. J. Geophys. Res. : Solid Earth 90 (B13), 11524–11532.

Bouton, J., Drack, E., Gardner, J., Prammer, M., 1996. Measurements of clay-bound water and total porosity by magnetic resonance logging. Log. Anal. 37 (6), 61–80.

Bultreys, T., De Boever, W., Cnudde, V., 2016. Imaging and image-based fluid transport modeling at the pore scale in geological materials: a practical introduction to the current state-of-the-art. Earth-Sci. Rev. 155, 93–128.

Cai, J., Perfect, E., Cheng, C.-L., Hu, X., 2014. Generalized modeling of spontaneous imbibition based on Hagen–Poiseuille flow in tortuous capillaries with variably shaped apertures. Langmuir 30 (18), 5142–5151.

Carman, P.C., 1997. Fluid flow through granular beds. Chem. Eng. Res. Des. 75, S32–S48.

Chalmers, G.R., Bustin, R.M., Power, I.M., 2012. Characterization of gas shale pore systems by porosimetry, pycnometry, surface area, and field emission scanning electron microscopy/transmission electron microscopy image analyses: examples from the Barnett, Woodford, Haynesville, Marcellus, and Doig units Characterization of Gas Shale Pore Systems. AAPG Bull. 96 (6), 1099–1119.

Chang, D., Vinegar, H.J., Morriss, C., Straley, C., 1994. Effective porosity, producible fluid and permeability in carbonates from NMR logging. In: SPWLA 35th Annual Logging Symposium (Tulsa, Oklahoma).

Churaev, N., 2003. Surface forces in wetting films. Colloid J. 65 (3), 263–274.

Clarkson, C.R., Bustin, R.M., 1996. Variation in micropore capacity and size distribution with composition in bituminous coal of the Western Canadian Sedimentary Basin: implications for coalbed methane potential. Fuel 75 (13), 1483–1498.

Clarkson, C.R., Jensen, J.L., Pedersen, P.K., Freeman, M., 2012. Innovative methods for flow-unit and pore-structure analyses in a tight siltstone and shale gas reservoir. AAPG Bull. 96 (2), 355–374.

Clarkson, C.R., Solano, N., Bustin, R.M., Bustin, A., Chalmers, G., He, L., Melnichenko, Y. B., Radliński, A., Blach, T.P., 2013. Pore structure characterization of North American shale gas reservoirs using USANS/SANS, gas adsorption, and mercury intrusion. Fuel 103, 606–616.

Cnudde, V., Boone, M.N., 2013. High-resolution X-ray computed tomography in geosciences: a review of the current technology and applications. Earth-Sci. Rev. 123, 1–17.

Coates, G.R., Xiao, L., Prammer, M.G., 1999. NMR Logging: Principles and Applications. Haliburton Energy Services, Houston.

Dai, Q., Luo, Q., Zhang, C., Lu, C., Zhang, Y., Lu, S., Zhao, Y., 2016. Pore structure characteristics of tight-oil sandstone reservoir based on a new parameter measured by NMR experiment: a case study of seventh Member in Yanchang Formation, Ordos Basin. Acta Petrol. Sin. 37 (7), 887–897 (in Chinese with English abstract).

Daigle, H., Dugan, B., 2009. Extending NMR data for permeability estimation in fine-grained sediments. Mar. Petrol. Geol. 26 (8), 1419–1427.

Daigle, H., Johnson, A., 2016. Combining mercury intrusion and nuclear magnetic resonance measurements using percolation theory. Transp. Porous Media 111 (3), 669–679.

Desbois, G., Urai, J.L., Kukla, P.A., Konstanty, J., Baerle, C., 2011. High-resolution 3D fabric and porosity model in a tight gas sandstone reservoir: a new approach to investigate microstructures from mm-to nm-scale combining argon beam cross-sectioning and SEM imaging. J. Petrol. Sci. Eng. 78 (2), 243–257.

Deutsch, C., 1989. Calculating effective absolute permeability in sandstone/shale sequences. SPE Form. Eval. 4 (3), 343–348.

Dong, H., Blunt, M.J., 2009. Pore-network extraction from micro-computerized-tomography images. Phys. Rev. E 80 (3), 036307.

Ferreol, B., Rothman, D.H., 1995. Lattice-Boltzmann simulations of flow through Fontainebleau sandstone. In: Multiphase Flow in Porous Media. Springer, Dordrecht.

Gallegos, D.P., Smith, D.M., 1988. A NMR technique for the analysis of pore structure: determination of continuous pore size distributions. J. Colloid Interface Sci. 122 (1), 143–153.

Gallegos, D.P., Munn, K., Smith, D.M., Stermer, D.L., 1987. A NMR technique for the analysis of pore structure: application to materials with well-defined pore structure. J. Colloid Interface Sci. 119 (1), 127–140.

Ge, X., Fan, Y., Zhu, X., Chen, Y., Li, R., 2014. Determination of nuclear magnetic resonance T_2 cutoff value based on multifractal theory—an application in sandstone with complex pore structure. Geophysics 80 (1), D11–D21.

Ghanbarian, B., Torres-Verdín, C., Lake, L.W., Marder, M., 2019. Gas permeability in unconventional tight sandstones: scaling up from pore to core. J. Petrol. Sci. Eng. 173, 1163–1172.

Giri, A., Tarafdar, S., Gouze, P., Dutta, T., 2012. Fractal pore structure of sedimentary rocks: simulation in 2-D using a relaxed bidisperse ballistic deposition model. J. Appl. Geophys. 87, 40–45.

Guo, B., Ghalambor, A., Duan, S., 2004. Correlation between sandstone permeability and capillary pressure curves. J. Petrol. Sci. Eng. 43 (3–4), 239–246.

Huang, H., Sun, W., Ji, W., Zhang, R., Du, K., Zhang, S., Ren, D., Wang, Y., Chen, L., Zhang, X., 2018. Effects of pore-throat structure on gas permeability in the tight sandstone reservoirs of the Upper Triassic Yanchang formation in the Western Ordos Basin, China. J. Petrol. Sci. Eng. 162, 602–616.

Hunt, A., Ewing, R., Ghanbarian, B., 2014. Percolation Theory for Flow in Porous Media, third eds. Springer, Heidelberg.

Israelachvili, J.N., 2011. Intermolecular and Surface Forces, third eds. Academic, London, p. 275. 416.

Jacquin, C.G., Adler, P., 1987. Fractal porous media II: geometry of porous geological structures. Transp. Porous Media 2 (6), 571–596.

Johnson, D.L., Koplik, J., Schwartz, L.M., 1986. New pore-size parameter characterizing transport in porous media. Phys. Rev. Lett. 57 (20), 2564–2567.

Johnson, E.A., Liu, S., Zhang, Y., 1989. Depositional environments and tectonic controls on the coal-bearing lower to middle jurassic yan'an formation, southern Ordos Basin, China. Geology 17 (12), 1123–1126.

Katz, A., Thompson, A., 1986. Quantitative prediction of permeability in porous rock. Phys. Rev. B 34 (11), 8179–8181.

Kaufmann, J., Loser, R., Leemann, A., 2009. Analysis of cement-bonded materials by multi-cycle mercury intrusion and nitrogen sorption. J. Colloid Interface Sci. 336 (2), 730–737.

Kleinberg, R.L., 1996. Utility of NMR T_2 distributions, connection with capillary pressure, clay effect, and determination of the surface relaxivity parameter ρ_2. Magn. Reson. Imaging 14 (7–8), 761–767.

Kolodzie Jr., S., 1980. Analysis of pore throat size and use of the Waxman-Smits equation to determine OOIP in Spindle Field, Colorado. In: SPE Annual Technical Conference and Exhibition. Dallas, Texas.

Kozeny, J., 1927. Über die kapillare Leitung des Wassers im Boden. Sitzungsber. Abt. IIa d. Math. naturwiss. Klasse der Wiener Akad. Wiss. 136, 271–306.

Lai, J., Wang, G., Fan, Z., Chen, J., Wang, S., Zhou, Z., Fan, X., 2016a. Insight into the pore structure of tight sandstones using NMR and HPMI measurements. Energy Fuels 30 (12), 10200–10214.

Lai, J., Wang, G.W., Ran, Y., Zhou, Z.L., Cui, Y.F., 2016b. Impact of diagenesis on the reservoir quality of tight oil sandstones: the case of Upper Triassic Yanchang Formation Chang 7 oil layers in Ordos Basin, China. J. Petrol. Sci. Eng. 145, 54–65.

Lai, J., Wang, G., Wang, Z., Chen, J., Pang, X., Wang, S., Zhou, Z., He, Z., Qin, Z., Fan, X., 2018. A review on pore structure characterization in tight sandstones. Earth-Sci. Rev. 177, 436–457.

Lai, J., Wang, G., Cao, J., Xiao, C., Wang, S., Pang, X., Dai, Q., He, Z., Fan, X., Yang, L., 2018b. Investigation of pore structure and petrophysical property in tight sandstones. Mar. Petrol. Geol. 91, 179–189.

Lebeau, M., Konrad, J.M., 2010. A new capillary and thin film flow model for predicting the hydraulic conductivity of unsaturated porous media. Water Resour. Res. 46 (12), W12554.

Li, J., Wang, S., Lu, S., Zhang, P., Cai, J., Zhao, J., Li, W., 2019. Microdistribution and mobility of water in gas shale: a theoretical and experimental study. Mar. Petrol. Geol. 102, 496–507.

Liang, Z., Ioannidis, M., Chatzis, I., 2000. Permeability and electrical conductivity of porous media from 3D stochastic replicas of the microstructure. Chem. Eng. Sci. 55 (22), 5247–5262.
Liu, Q., Jin, Z., Meng, Q., Wu, X., Jia, H., 2015. Genetic types of natural gas and filling patterns in Daniudi gas field, Ordos Basin, China. J. Asian Earth Sci. 107, 1–11.
Liu, J.Q., Zhang, C.M., Zhang, Z.S., 2016. Combine the capillary pressure curve data with the porosity to improve the prediction precision of permeability of sandstone reservoir. J. Petrol. Sci. Eng. 139, 43–48.
Liu, X., Wang, J., Ge, L., Hu, F., Li, C., Li, X., Yu, J., Xu, H., Lu, S., Xue, Q., 2017. Pore-scale characterization of tight sandstone in Yanchang Formation Ordos Basin China using micro-CT and SEM imaging from nm-to cm-scale. Fuel 209, 254–264.
Lock, P.A., Jing, X., Zimmerman, R.W., Schlueter, E.M., 2002. Predicting the permeability of sandstone from image analysis of pore structure. J. Appl. Phys. 92 (10), 6311–6319.
Lonnes, S., Guzman-Garcia, A., Holland, R., 2003. NMR petrophysical predictions on cores. In: SPWLA 44th Annual Logging Symposium. Dallas, Texas.
Mandelbrot, B.B., 1975. Les objets fractals: forme, hasard et dimension. Flammarion, Paris.
Mandelbrot, B.B., Passoja, D.E., Paullay, A.J., 1984. Fractal character of fracture surfaces of metals. Nature 308 (5961), 721–722.
Mao, Z.Q., Xiao, L., Wang, Z.N., Jin, Y., Liu, X.G., Xie, B., 2013. Estimation of permeability by integrating nuclear magnetic resonance (NMR) logs with mercury injection capillary pressure (MICP) data in tight gas sands. Appl. Magn. Reson. 44 (4), 449–468.
Martin, P., Dacy, J., 2004. Effective Qv by NMR core tests. In: SPWLA 45th Annual Logging Symposium. Noordwijk, Netherlands.
Mees, F., Swennen, R., Van Geet, M., Jacobs, P., 2003. Applications of X-ray computed tomography in the geosciences. Geol. Soc. London, Spec. Publ. 215, 1–6.
Nelson, P.H., 1994. Permeability-porosity relationships in sedimentary rocks. Log. Anal. 35 (3), 38–62.
Pape, H., Clauser, C., Iffland, J., 1999. Permeability prediction based on fractal pore-space geometry. Geophysics 64 (5), 1447–1460.
Pittman, E.D., 1992. Relationship of porosity and permeability to various parameters derived from mercury injection-capillary pressure curves for sandstone. AAPG Bull. 76 (2), 191–198.
Purcell, W., 1949. Capillary pressures-their measurement using mercury and the calculation of permeability therefrom. J. Petrol. Technol. 1 (2), 39–48.
Qiao, J., Zeng, J., Jiang, S., Feng, S., Feng, X., Guo, Z., Teng, J., 2019a. Heterogeneity of reservoir quality and gas accumulation in tight sandstone reservoirs revealed by pore structure characterization and physical simulation. Fuel 253, 1300–1316.
Qiao, J., Zhao, X., Zeng, J., Han, G., Jiang, S., Feng, S., Feng, X., 2019b. The impacts of nano-micrometer pore structure on the gas migration and accumulation in tight sandstone gas reservoirs. Energies 12 (12), 4102.
Qiao, J., Zeng, J., Jiang, S., Ma, Y., Feng, S., Xie, H., Wang, Y., Hu, H., 2020a. Role of pore structure in the percolation and storage capacities of deeply buried sandstone reservoirs: a case study of the Junggar Basin. China. Mar. Petrol. Geol. 113, 104129.
Qiao, J., Zeng, J., Jiang, S., Wang, Y., 2020b. Impacts of sedimentology and diagenesis on pore structure and reservoir quality in tight oil sandstone reservoirs: implications for macroscopic and microscopic heterogeneities. Mar. Petrol. Geol. 111, 279–300.
Qiao, J., Zeng, J., Jiang, S., Zhang, Y., Feng, S., Feng, X., Hu, H., 2020c. Insights into the pore structure and implications for fluid flow capacity of tight gas sandstone: a case study in the upper paleozoic of the Ordos Basin. Mar. Petrol. Geol. 118, 104439.
Qiao, J., Zeng, J., Ma, Y., Jiang, S., Feng, S., Hu, H., 2020d. Effects of mineralogy on pore structure and fluid flow capacity of deeply buried sandstone reservoirs with a case study in the Junggar Basin. J. Petrol. Sci. Eng. 189, 106986.
Rezaee, R., Saeedi, A., Clennell, B., 2012. Tight gas sands permeability estimation from mercury injection capillary pressure and nuclear magnetic resonance data. J. Petrol. Sci. Eng. 88, 92–99.
Ross, D.J., Bustin, R.M., 2007. Impact of mass balance calculations on adsorption capacities in microporous shale gas reservoirs. Fuel 86 (17–18), 2696–2706.
Ross, D.J., Bustin, R.M., 2009. The importance of shale composition and pore structure upon gas storage potential of shale gas reservoirs. Mar. Petrol. Geol. 26 (6), 916–927.
Sakhaee-Pour, A., Bryant, S.L., 2014. Effect of pore structure on the producibility of tight-gas sandstones. AAPG Bull. 98 (4), 663–694.
Sheng, G., Su, Y., Zhao, H., Liu, J., 2020. A unified apparent porosity/permeability model of organic porous media: coupling complex pore structure and multi-migration mechanism. Adv. Geo-Energy Res. 4 (2), 115–125.
Soeder, D., Chowdiah, P., 1990. Pore geometry in high-and low-permeability sandstones, travis peak formation, east Texas. SPE Form. Eval. 5 (4), 421–430.
Sok, R.M., Knackstedt, M.A., Varslot, T., Ghous, A., Latham, S., Sheppard, A.P., 2010. Pore scale characterization of carbonates at multiple scales: integration of Micro-CT, BSEM, and FIBSEM. Petrophysics 51 (6), 379–387.
Spanne, P., Thovert, J., Jacquin, C., Lindquist, W., Jones, K., Adler, P., 1994. Synchrotron computed microtomography of porous media: topology and transports. Phys. Rev. Lett. 73 (14), 2001–2004.
Swanson, B., 1981. A simple correlation between permeabilities and mercury capillary pressures. J. Petrol. Technol. 33 (12), 2498–2504.
Thomas, R.D., Ward, D.C., 1972. Effect of overburden pressure and water saturation on gas permeability of tight sandstone cores. J. Petrol. Technol. 24 (2), 120–124.
Thomeer, J., 1960. Introduction of a pore geometrical factor defined by the capillary pressure curve. J. Petrol. Technol. 12 (3), 73–77.
Thomeer, J., 1983. Air permeability as a function of three pore-network parameters. J. Petrol. Technol. 35 (4), 809–814.
Tiab, D., Donaldson, E.C., 2015. In: Petrophysics: Theory and Practice of Measuring Reservoir Rock and Fluid Transport Properties. Gulf Professional Publishing, America.
Tian, W., Lu, S., Huang, W., Wang, W., Li, J., Gao, Y., Zhan, Z., Sun, Y., 2020. Quantifying the control of pore types on fluid mobility in low-permeability conglomerates by integrating various experiments. Fuel 275, 117835.
Tuller, M., Or, D., 2003. Hydraulic functions for swelling soils: pore scale considerations. J. Hydrol. 272 (1–4), 50–71.
Wang, Y., Zhu, Y., Chen, S., Li, W., 2014. Characteristics of the nanoscale pore structure in Northwestern Hunan shale gas reservoirs using field emission scanning electron microscopy, high-pressure mercury intrusion, and gas adsorption. Energy Fuels 28, 945–955.
Wang, Y., Zhu, Y., Liu, S., Zhang, R., 2016. Pore characterization and its impact on methane adsorption capacity for organic-rich marine shales. Fuel 181, 227–237.
Wells, J., Amaefule, J., 1985. Capillary pressure and permeability relationships in tight gas sands. In: SPE/DOE Low Permeability Gas Reservoirs Symposium. Denver, Colorodo.
Westphal, H., Surholt, I., Kiesl, C., Thern, H.F., Kruspe, T., 2005. NMR measurements in carbonate rocks: Problems and an approach to a solution. Pure Appl. Geophys. 162 (3), 549–570.
Wong, P.Z., Koplik, J., Tomanic, J., 1984. Conductivity and permeability of rocks. Phys. Rev. B 30 (11), 6606–6614.
Woodruff, W., Revil, A., 2011. CEC-normalized clay-water sorption isotherm. Water Resour. Res. 47 (11), W11502.
Wu, H., Ji, Y.L., Liu, R., Zhang, C.L., Chen, S., 2017. Insight into the pore structure of tight gas sandstones: a case study in the Ordos Basin, NW China. Energy Fuels 31 (12), 13159–13178.
Xia, Y., Cai, J., Perfect, E., Wei, W., Zhang, Q., Meng, Q., 2019. Fractal dimension, lacunarity and succolarity analyses on CT images of reservoir rocks for permeability prediction. J. Hydrol. 579, 124198.
Xiao, L., Mao, Z.Q., Wang, Z.N., Jin, Y., 2012. Application of NMR logs in tight gas reservoirs for formation evaluation: a case study of Sichuan basin in China. J. Petrol. Sci. Eng. 81, 182–195.
Xiao, D.S., Lu, S.F., Yang, J.X., Zhang, L.C., Li, B., 2017a. Classifying multiscale pores and investigating their relationship with porosity and permeability in tight sandstone gas reservoirs. Energy Fuels 31 (9), 9188–9200.
Xiao, L., Liu, D., Wang, H., Li, J., Lu, J., Zou, C., 2017b. The applicability analysis of models for permeability prediction using mercury injection capillary pressure (MICP) data. J. Petrol. Sci. Eng. 156, 589–593.
Xiao, D., Jiang, S., Thul, D., Lu, S., Zhang, L., Li, B., 2018. Impacts of clay on pore structure, storage and percolation of tight sandstones from the Songliao Basin, China: implications for genetic classification of tight sandstone reservoirs. Fuel 211, 390–404.
Yang, S., Yu, Q., 2020. Experimental investigation on the movability of water in shale nanopores: a case study of carboniferous shale from the qaidam basin, China. Water Resour. Res. 56 (8), e2019WR026973.
Yang, R., He, S., Yi, J., Hu, Q., 2016a. Nano-scale pore structure and fractal dimension of organic-rich Wufeng-Longmaxi shale from Jiaoshiba area, Sichuan Basin: investigations using FE-SEM, gas adsorption and helium pycnometry. Mar. Petrol. Geol. 70, 27–45.
Yang, Z., He, S., Guo, X., Li, Q., Chen, Z., Zhao, Y., 2016b. Formation of low permeability reservoirs and gas accumulation process in the daniudi gas field, northeast Ordos Basin, China. Mar. Petrol. Geol. 70, 222–236.
Yao, Y., Liu, D., 2012. Comparison of low-field NMR and mercury intrusion porosimetry in characterizing pore size distributions of coals. Fuel 95, 152–158.
Yao, Y., Liu, D., Che, Y., Tang, D., Tang, S., Huang, W., 2009. Non-destructive characterization of coal samples from China using microfocus X-ray computed tomography. Int. J. Coal Geol. 80 (2), 113–123.
Yao, Y., Liu, D., Che, Y., Tang, D., Tang, S., Huang, W., 2010. Petrophysical characterization of coals by low-field nuclear magnetic resonance (NMR). Fuel 89 (7), 1371–1380.
Yuan, Y., Rezaee, R., 2019a. Fractal analysis of the pore structure for clay bound water and potential gas storage in shales based on NMR and N2 gas adsorption. J. Petrol. Sci. Eng. 177, 756–765.
Yuan, Y., Rezaee, R., 2019b. Impact of paramagnetic minerals on NMR-converted pore size distributions in Permian Carynginia shales. Energy Fuels 33 (4), 2880–2887.
Yuan, H., Swanson, B., 1989. Resolving pore-space characteristics by rate-controlled porosimetry. SPE Form. Eval. 4 (1), 17–24.
Yuan, Y., Rezaee, R., Verrall, M., Hu, S.-Y., Zou, J., Testmanti, N., 2018. Pore characterization and clay bound water assessment in shale with a combination of NMR and low-pressure nitrogen gas adsorption. Int. J. Coal Geol. 194, 11–21.
Zeng, J., Feng, X., Feng, S., Zhang, Y., Qiao, J., Yang, Z., 2017. Influence of tight sandstone micro-nano pore-throat structures on petroleum accumulation: evidence from experimental simulation combining x-ray tomography. J. Nanosci. Nanotechnol. 17 (9), 6459–6469.

Zha, W., Yan, S., Li, D., Lu, D., 2017. A study of correlation between permeability and pore space based on dilation operation. Adv. Geo-Energy Res. 1 (2), 93–99.
Zhao, H.W., Ning, Z.F., Wang, Q., Zhang, R., Zhao, T.Y., Niu, T.F., Zeng, Y., 2015. Petrophysical characterization of tight oil reservoirs using pressure-controlled porosimetry combined with rate-controlled porosimetry. Fuel 154, 233–242.
Zhao, H., Ning, Z., Zhao, T., Zhang, R., Wang, Q., 2016. Effects of mineralogy on petrophysical properties and permeability estimation of the Upper Triassic Yanchang tight oil sandstones in Ordos Basin, Northern China. Fuel 186, 328–338.
Zhao, Y., Sun, Y., Liu, S., Wang, K., Jiang, Y., 2017. Pore structure characterization of coal by NMR cryoporometry. Fuel 190, 359–369.
Zhao, X., Zheng, D., Xie, G., Jenkyns, H.C., Guan, C., Fang, Y., He, J., Yuan, X., Xue, N., Wang, H., Li, S., Jarzembowski, E.A., Zhang, H., Wang, B., 2020. Recovery of lacustrine ecosystems after the end-Permian mass extinction. Geology 48 (6), 609–613.
Zisser, N., Kemna, A., Nover, G., 2010. Relationship between low-frequency electrical properties and hydraulic permeability of low-permeability sandstones. Geophysics 75 (3), E131–E141.